3-11-2011

Characterization of the Neutron Spectrum at the Indiana University NREP Neutron Source

Matthew R. Halstead

Follow this and additional works at: https://scholar.afit.edu/etd

Part of the Nuclear Commons

CHARACTERIZATION OF THE ENERGY SPECTRUM AT THE INDIANA UNIVERSITY NREP NEUTRON SOURCE

THESIS

Matthew R. Halstead, Civilian

AFIT/GNE/ENP/11-M08

DEPARTMENT OF THE AIR FORCE
AIR UNIVERSITY

AIR FORCE INSTITUTE OF TECHNOLOGY

Wright-Patterson Air Force Base, Ohio

APPROVED FOR PUBLIC RELEASE; DISTRIBUTION UNLIMITED

The views expressed in this document are those of the author and do not reflect the official policy or position of the United States Air Force, the United States Department of Defense or the United States Government. This material is declared a work of the U.S. Government and is not subject to copyright protection in the United States.

CHARACTERIZATION OF THE ENERGY SPECTRUM

AT THE INDIANA UNIVERSITY NREP NEUTRON SOURCE

THESIS

Presented to the Faculty

Department of Engineering Physics

Graduate School of Engineering and Management

Air Force Institute of Technology

Air University

Air Education and Training Command

in Partial Fulfillment of the Requirements for the

Degree of Master of Science in Nuclear Engineering

Matthew R. Halstead, B.S.Nuc.E., B.S.M.E.

Civilian

March, 2011

APPROVED FOR PUBLIC RELEASE; DISTRIBUTION UNLIMITED

AFIT/GNE/ENP/11-M08

CHARACTERIZATION OF THE ENERGY SPECTRUM

AT THE INDIANA UNIVERSITY NREP NEUTRON SOURCE
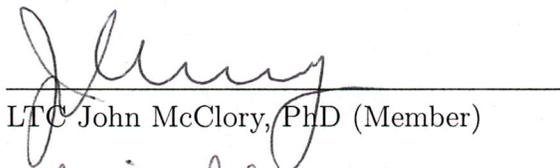
Matthew R. Halstead, B.S.Nuc.E., B.S.M.E.
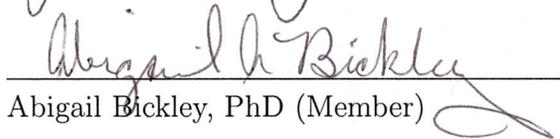Civilian

Approved:

_____
James Petrosky, PhD (Chairman)

_____
Date

11 Mar 11

_____
LTC John McClory, PhD (Member)

_____
Date

4 MAR 11

_____
Abigail Bickley, PhD (Member)

_____
Date

10 Mar 11

Abstract

The neutron source at the Indiana University Cyclotron Facility produces neutrons via proton bombardment of a natural beryllium (100% ^{9}Be) target. This source has two beam lines: the LENS and the NREP. The energy spectrum of the neutrons produced on the NREP beam line has not yet been characterized. Through simulation using the GEANT and MCNP particle transport codes as well as neutron activation analysis experiments, an attempt was made to characterize the energy spectrum of the neutron production source. First, the neutron production spectrum of beryllium, simulated using GEANT, was compared with literature; there are significant deviations. Next, foils and wires of pure elements were irradiated in the neutron beam target area and the resulting gamma spectrum measured. This information was used in an unfolding code, SAND-II, to deconvolve the neutron energy spectrum observed at the target. A number of approximations were made to properly account for beam duty time and neutron production anisotropy. The resultants provide a better understanding of the spectrum, but continued work is needed to produce a useful spectrum for the users of the facility.

Acknowledgements

Table of Contents

List of Figures

List of Tables

	Table		Page

List of Abbreviations

CHARACTERIZATION OF THE ENERGY SPECTRUM
AT THE INDIANA UNIVERSITY NREP NEUTRON SOURCE

I. Introduction

The purpose of this thesis was to quantify the neutron spectrum produced at the Neutron Radiation Effects Program (NREP) beam line at the Indiana University (IU) Cyclotron Facility. To do so, six methods of neutron spectroscopy were investigated. Neutron activation analysis was chosen as the best and most achievable form. A well-defined neutron spectrum is critical to the use of any facility as a neutron irradiation source. Currently, end-users in the Department of Defense (DoD), Department of Energy (DOE), and other national and international organizations utilize the facility for neutron irradiation studies. However, the spectrum is not fully characterized and can only be approximated based on knowledge of the neutron-production reactions and Monte Carlo simulations. Many of the users of this facility seek to test electrical components for their survivability in adverse neutron radiation environments. The goal of this work is to measure the spectrum so that the IU neutron source can become a more useful irradiation source for the end-user.

1.1   Motivation

Even though the global political environment is no longer dominated by two superpowers on the brink of nuclear war, the threat of nuclear weapon use is greater than ever [4]. The rise of international terrorist organizations with the motive and the means to procure nuclear weapons or weapon material lends increased credibility to the likelihood of nuclear detonation. Despite this, the national capability to

test and evaluate electrical components in a variety of radiation environments continues to degrade as experts retire and equipment is decommissioned and dismantled. For many years, the United States relied on three main fast-burst research reactors for validation: the Sandia Pulsed Reactor (SPR-III) at Sandia National Laboratory (SNL), the U.S. Army Pulsed Reactor Facility (APRF) at Aberdeen Proving Ground, and the Fast Burst Reactor (FBR) at the White Sands Missile Range (WSMR).

The SPR-III was a "Godiva-type" fast-burst research reactor developed by SNL in the 1970s. The primary purpose was verification and validation studies of electrical components in radiation environments [21]. The third generation of this reactor, SPR-III, possessed an expansive internal irradiation volume, which was a unique feature for irradiation facilities. Equipment to be tested was placed in a facility called a *kiva*. This kiva gave experimenters a place for large items to be irradiated outside the core without damage to them or associated measurement equipment [9]. In addition, it was one of the only test facilities in the world that could produce radiation pulses that closely simulated nuclear weapon environments. Security concerns regarding the highly enriched uranium fuel led to the dismantling of SPR-III as well as the APRF.

With the dismantling of SPR-III in 2007 [3], a pressing need has arisen to find facilities capable of simulating the pulsed radiation environments produced by nuclear weapons. In the past, SPR-III and the other two fast burst reactors had been used to analyze the electrical component damage induced by neutron and gamma irradiation. The results of this analysis validated many of the components currently in use in United States nuclear weapon systems. In order to ensure the continued capability to test and evaluate these components, the Indiana University Cyclotron Facility's neutron source may be capable of being used to simulate portions of these radiation environments.

2

1.2 Background & Facility Description

1.2.1 Facility Description
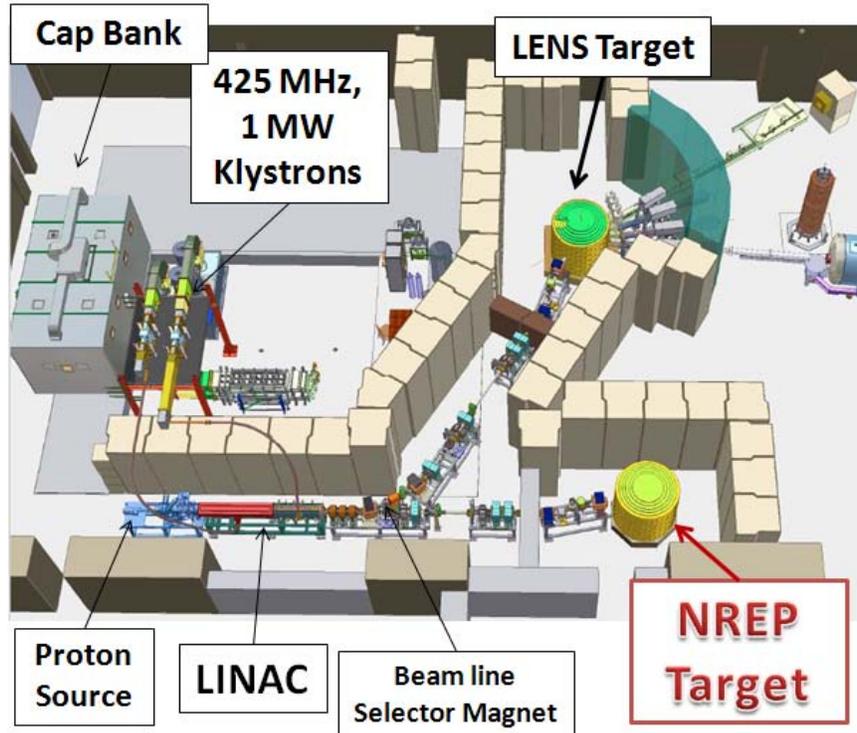
Figure 1. The IU LINAC Facility schematic shows the proton source and LINAC at bottom left; the beam is split to targets in lower right and upper middle; and the 425 MHz, 1 MW klystron power source with capacitor bank is in upper left [32].

At the IU Center for Exploration of Energy and Matter (CEEM), there is a pulsed neutron source that produces neutrons via the inelastic scattering of protons on beryllium. Figure 1 shows a schematic view of the facility. Protons are created in an ion source, then are accelerated and directed onto a target assembly inside a moderator/reflector stack where neutrons are created. Each of these steps will now be explained in greater detail.

The protons are created by stripping an electron from elemental hydrogen in the

ion source, displayed in the lower left corner of Figure 1. These protons are collected and focused into a 3 MeV Radio Frequency Quadrupole (RFQ) accelerator directly coupled to two Drift Tube LINACs (DTL), which accelerate protons to their final energy of 13 MeV. Proton acceleration is facilitated by three Litton 5773 klystron RF tubes that provide 425 MHz microwave power to the RFQ and DTL components. Power delivered to the LINAC is approximately 1 MW with a 0.9% duty factor [10]. The duty factor is a measure of the time a pulsed beam is running. In essence, the duty factor can be described by $DF = \frac{PW}{t_{cycle}}$ where PW = pulse width and t_{cycle} is the total time for one pulse cycle, which includes one proton pulse and one recovery period, and is defined as $t_{cycle} = f^{-1}$ where f is the accelerator frequency. The typical beam operating frequency is 20 Hz, making $t_{cycle} = 50ms$.

After acceleration, the protons are focused using octupole magnets and directed down one of two beam lines using a selector magnet. The existence of two beam lines gives the facility increased flexibility in experiment set-up and operation. The first beam line is called the Low-Energy Neutron Source (LENS) beam line, while the second is called the Neutron Radiation Effects Program (NREP) beam line. Neutron production at the LENS target has been analyzed extensively [25], however the moderator configuration makes the LENS target impractical for use in radiation effects studies. Therefore, the focus of this research is the characterization of the NREP beam line neutron energy spectrum.

The NREP beam line terminates on a Target-Moderator-Reflector (TMR) stack, which contains a beryllium target assembly, space for a moderator containment vessel, and external shielding. The shielding primarily consists of borated polyethylene bricks to absorb neutrons and lead to absorb gamma radiation, with the goal of limiting radiation exposure outside the TMR.

4

1.2.2 Ion Beam Fundamentals

The RFQ, which was proposed by Kapchinskiy and Teplikov in 1969 [20], accelerates ions (in this case, protons) to approximately 1-6% of c, the speed of light, for injection into the DTL system. They then enter the DTL to be accelerated to their final energy. In the DTL, the H^+ ions travel a distance in an electric field that accelerates them. However, because the system is powered by an intense microwave beam with an alternating current, the ions must travel next through a tube acting as a Faraday cage, acting to suppress external fields. Within this cage, the ions are allowed to drift under vacuum without being slowed by the electric field. After leaving the cage, they are again accelerated by the electric field. An illustration of this procedure is displayed in Figure 2. This is repeated for the length required to reach the necessary velocity [41]. In the case of the IU LINAC, the final velocity of the protons is 7-13 MeV.
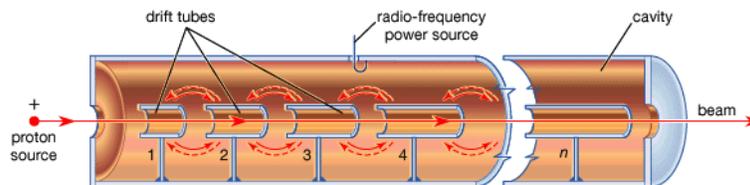
Figure 2. The schematic representation is of a Drift Tube LINAC where ions are accelerated using electric fields and Faraday shields.

After acceleration in the LINAC, the protons are directed to a target station where a small fraction interact via the $(H^+ + {}^9Be \to xn + \ldots)$ reaction, which produces neutrons of various energies. This neutron production spectrum will be discussed further in Section 2.1.

There is one major difference between the LENS and NREP beam lines. At the LENS beam line, neutrons produced in the target travel through a moderator region

made up of liquid methane before reaching the location where they are measured. This moderator has a high cross section for scattering interactions because of the four hydrogen atoms per molecule. The methane moderator induces a shift in the neutron energy spectrum to lower energies, which is called *softening* the spectrum. However, in the NREP beam line being analyzed in this research, the methane moderator is not present. Neutrons can still be slowed down and reflected back into the target area by other materials in the TMR stack, but a *harder* spectrum that more closely reflects the neutron "birth" energy spectrum is expected.

1.2.3 Neutron Energy Spectrum Molding

The neutron spectrum of interest for radiation hardness testing of electronics in nuclear weapon environments has a much larger fast neutron component than a water-moderated reactor or the IU neutron source, as currently configured. A typical nuclear weapon neutron energy spectrum, as calculated in Glasstone and Dolan [15], is displayed on the right in Figure 3. It is compared with the neutron birth spectrum from 5 MeV protons impacting beryllium presented in work done by Howard *et al.* [18]. To make a comparison with past verification and validation work done at the SPR-III facility, it may be necessary in the future to mold the neutron energy spectrum found at the NREP beam line in order to optimize total flux and energy spectrum characteristics. This may be accomplished by changing the target material composition from beryllium to another material, optimizing the target geometry to increase neutron flux at the target location, changing the TMR composition to include different moderator materials, or other modifications to be determined later.
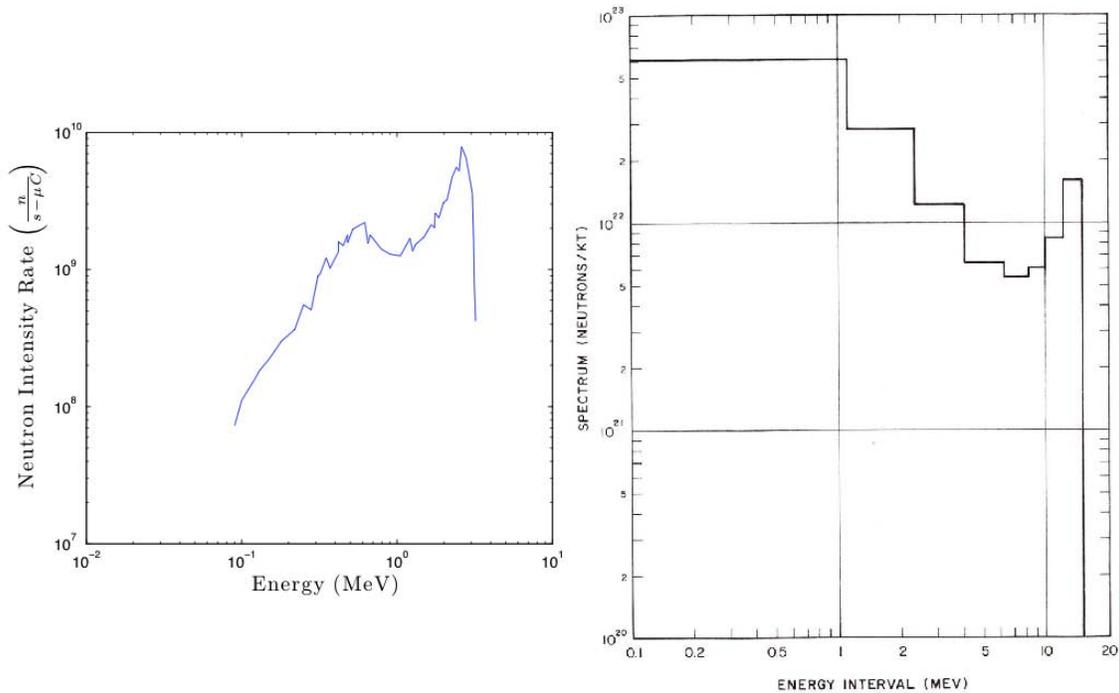
Figure 3. <u>Left:</u> Howard *et al.* [18] presented the neutron spectrum produced by impacting 5 MeV protons in beryllium. <u>Right:</u> Glasstone and Dolan [15] presented the typical neutron intensity spectrum expected from a nuclear weapon blast, integrated over the total blast time interval.

1.3 Problem Statement

The neutron energy spectrum at the IU CEEM neutron source's NREP beam line is not well characterized. Currently, the source's primary purpose is to study low-energy neutron interactions using the LENS beam line. In past studies, flux measurements were accomplished using gold foils for measurement of the thermal region and sulfur pellets and nickel foils for neutrons of energy greater than 3 MeV [33]. However, this was only accomplished on the LENS beam line. To correlate the NREP neutron environment to the environments simulated by the SPR-III reactor, the entire neutron energy spectrum of the NREP beam line must be well characterized.

7

1.4 Approach

This work follows two paths. A model of the neutron beam facility was built using the particle transport code, GEANT [5]. This simulation environment, in conjunction with computer analysis done in MCNP [13] and input by IU researchers ([26],[27]), provided an estimate of the expected spectrum. The spectrum was then measured by multiple-element neutron activation analysis. A high-purity germanium detector with associated gamma measurement software was used to measure the induced gamma activity spectrum in each sample material. The resulting activity data provided input data into a spectrum unfolding code, Spectrum Analysis by Neutron Detectors, Version 2 (SAND-II). The GEANT simulation results provided the initial input guess for the SAND-II routines. The spectrum produced by the SAND-II code will be representative of the neutron flux produced in the NREP beam line.

A spectrum similar to the $^9Be(p,n)$ neutron birth spectrum is expected. Some perturbations due to scattering and reflection could soften the spectrum. However, the lack of a strong moderator, such as liquid methane found in the LENS beam line TMR, should preclude significant modification.

II. Theory and Neutron Spectrometry Review

At the facility studied in this work, neutrons are produced via inelastic scattering of protons on beryllium targets. Before beginning experiment and simulation, many potential options available for neutron spectroscopy were studied. In this section, neutron production methods in beryllium are reviewed, a number of the methods of quantifying neutron energy spectra are discussed, the GEANT code methodology is described, and the theory underlying the multiple-element neutron activation analysis method is detailed.

2.1 ^{9}Be(p,n) Production Methods

At an incident proton energy of 13 MeV, inelastic scattering of protons in beryllium is the dominant method by which neutrons are produced. Despite experimental work showing the expected neutron production spectra for incident proton energies of 3.0-5.0 MeV [18], 17.24 MeV [12], or 35 MeV [6], there is a significant lack of experimental information in the 7-13 MeV range. Figure 4 displays the neutron production spectrum for various proton energies between 3.0 and 5.0 MeV as found by Howard *et al.* [18].

There are three main channels of neutron production via inelastic scattering at the incident proton energies of interest [25]. The three channels are compound nucleus break-up, direct-charge exchange, and multi-body break-up. The first channel, compound nucleus break up, is the dominant avenue for the production of high energy neutrons and is thought to produce the peak at the right of the spectrum displayed in Figure 4. Multi-body break-up imparts less energy to the neutron due to conservation of momentum in the system, and thus it contributes strongly to the low-energy component of the spectrum. As the incident energy of the proton increases, there are
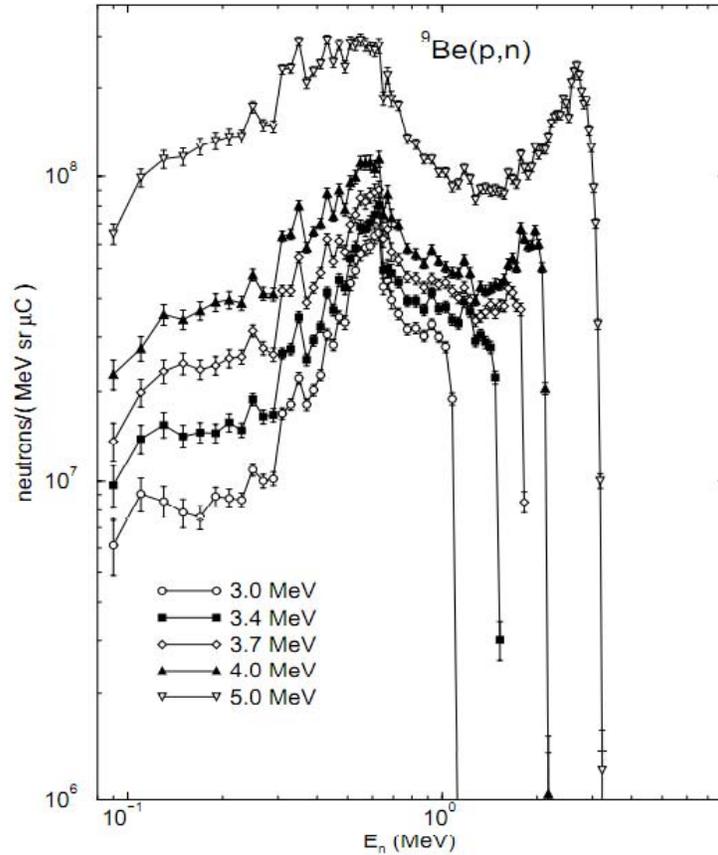
Figure 4. Howard *et al.* [18] produced neutron spectra for a variety of low energy bombarding protons in beryllium.

more excited states of the compound nucleus decaying to the ground state by emitting mid-energy neutrons. This begins to fill in the "valley" between the multi-body break up peak at 0.6 MeV and the peak due to compound nucleus break up. Additionally, while the break up mechanisms are considered isotropic, direct-charge exchange is noted to be biased in the forward-scattering direction. This will be discussed further in Section 3.3.2.3.

2.2 Neutron Spectrometry

2.2.1 Bonner Sphere Spectroscopy

A radiation measurement device called a Bonner Sphere Spectrometer (BSS) [11] uses multiple, concentric spherical moderators of various sizes, which surround thermal neutron counters such as europium-doped lithium iodide scintillator detectors or BF_3 proportional detectors. Each detector produces a counting curve that, when combined with all others, can be unfolded into a neutron spectrum. This can be accomplished using an understanding of how the neutrons are slowed as they traverse the moderating spheres.

The main advantages of Bonner spheres are their simplicity, portability, and wide energy range coverage. They benefit from decades of use, such that the resultant counting curves can be easily unfolded and interpreted. In addition to the ease-of-use, Bonner spheres are relatively insensitive to gamma rays. By setting the discriminator level properly, gamma interactions can be ignored and not counted, leading to higher signal-to-noise ratios and better counting statistics.

The main disadvantages of Bonner spheres are low energy resolution between 10^{-3} and 10^2 keV and that various spheres have sensitivity peaks at different neutron energies. In addition, Bonner spheres have a stronger response to neutrons at higher energies than those at lower energies, which can degrade the energy resolution at lower energies due to low count rates.

This spectrographic method was strongly considered for measuring the IU NREP neutron energy spectrum, due to its numerous advantages balanced by relatively few disadvantages. The decision to use neutron activation analysis was made based on a decision that irradiation foils would be easier to procure than a BSS. In addition, the Bonner spheres could not fit inside the TMR internal cavity. Therefore, the spectrum would need to be measured outside the TMR stack via a port, which may not be

11

indicative of the spectrum at the potential site for radiation effects on electronics studies.

2.2.2 Rotating Spectrometer

Another spectroscopy system studied was a Rotating Spectrometer (ROSPEC). ROSPEC is a system similar to the BSS in that it is a collection of multiple detectors optimized to detect neutrons within a specified energy range. It is a completely self-contained unit that measures neutron energy via recoiling protons in gas proportional counters. The resultant data streams are collected and unfolded by a controlling algorithm to provide a neutron spectrum [2]. Similar to the BSS, incident gamma irradiation can be rejected due to much lower pulse heights. An example of a ROSPEC, built by Bubble Technologies Inc., is displayed in Figure 5. The base system is capable of determining neutron spectra from 50 keV to 5 MeV. With the addition of two Helium tubes that are capable of detecting and measuring thermal neutrons as well as an external plastic scintillator that counts fast neutrons, the ROSPEC system can operate in a range of 0.01 eV to 17 MeV. This is adequate for the the NREP beam line.

ROSPEC was not used in this research for a number of reasons. ROSPEC is considered a *turn-key* system, in that all necessary components for spectral unfolding are contained in the platform. While this may help determine a spectrum quickly in most situations, it can also be considered a major disadvantage for a researcher. It becomes a "black box" system, one whose operation is not easily changed. The unfolding algorithm is proprietary, so the researcher is forced to assume that the results are reliable based on the claims of the company that produced the ROSPEC. The major reason why ROSPEC was not used is the great cost and lead time involved with procuring one of the devices. When compared to the low-cost and immediate

12

Figure 5. The ROSPEC is a completely self-contained neutron spectrometry system capable of measuring neutron energies from thermal through fast.

availability of activation foils, ROSPEC was not considered feasible for this work. Also, similar to the Bonner spheres, the ROSPEC could not fit inside the internal TMR cavity.

2.2.3   Superheated Drop Detector

Another method of measuring a neutron source spectrum is to use Superheated Drop Detectors (SDD) in a spectrometer known as a Bubble Interactive Neutron Spectrometer (BINS). Neutrons impinge on a detector containing superheated liquid droplets, usually halocarbons, suspended within a semi-solid medium.

Superheated liquids are those that are heated past their boiling point, but are still in the liquid phase. A small amount of energy can cause the metastable superheated

droplets to gasify, creating a bubble. Once created, the bubbles are counted, either visually or with a specially-designed reader, to give a measure of the number and energy of the incident neutrons. One such reader is displayed in Figure 6. Inside a detector vial, the semi-solid material usually is an aqueous or polymeric gel. The vial is sealed to maintain static pressure on the composition and is stored at lower temperature prior to use. An example of a superheated drop detector is displayed in Figure 6.

Figure 6. <u>Left:</u> **The SDD is a vial of gelatinous liquid containing superheated drops that neutrons interact with, causing voids that can be counted.** <u>Right:</u> **The SDD reader is an easy way to count the voids created by neutrons in a superheated drop detector.**

Neutrons incident on a SDD interact with the superheated droplets and cause them to expand [38]. This is based on the concept of *nucleation.* Neutrons deposit energy in the halocarbon droplets [36], and a bubble is formed if the energy deposited is greater than a threshold value of W,

$$W = \frac{16\pi\gamma^3(T)}{3\left(p_v - p_o\right)^2},\tag{1}$$

14

where $\gamma(T)$ is the surface tension between liquid and vapor, p_v is the vapor pressure of the superheated liquid and p_o is the ambient pressure. The difference between p_v and p_o is sometimes called the *degree of superheat* of the liquid. Equation 1 describes the minimum, or threshold, energy required to create a bubble. However, γ changes with temperature. Therefore, the threshold changes as well.

The BINS spectrometer uses SDD and is based on this principle. By varying the temperature, the SDD will respond to different neutron energy regimes [39]. Mixed spectra are produced that can then be deconvolved using computer codes such as SAND-II and MAXED [35].

The main advantages of the BINS system are the wide energy range coverage and its complete insensitivity to gamma irradiation. The disadvantages include the tedious manual counting methods, which can be mitigated by the reader in Figure 6, and temperature change limitations. Changes in temperature cause threshold changes which can negatively impact spectral results.

This spectrometric method was not chosen for a number of reasons. The strict temperature requirement would have forced the detectors to be monitored for temperature change, and a heat addition/removal system would need to be designed to maintain detector temperature. Additionally, neither the bubble detectors nor the reader were easily available, so the money and time for procurement was prohibitive, as well.

2.2.4 Time of Flight

Another method of determining neutron energy spectra is Time-of-Flight (ToF) spectroscopy. This method of spectroscopy makes use of the differences in particle arrival time as a function of the particle's kinetic energy. The velocity of a particle,

v, can be described as

$$v = c \left[1 - \left(\frac{1}{1 + \frac{KE}{m_o c^2}} \right)^2 \right]^{\frac{1}{2}}, \tag{2}$$

where m_o is the rest mass of the particle (939.565 MeV/c^2 for a neutron), v is the velocity, and c is the speed of light in the medium. The kinetic energy, KE, must be treated relativistically because a 10 MeV neutron travels at 15% of the speed of light. The classical representation, $KE = \frac{1}{2}mv^2$, would have an error of approximately 2%. On the other hand, a 0.1 MeV neutron travels at only 1.5% of the speed of light. For this reason, neutrons can be discriminated as a function of energy based on the time required to travel a given distance. This can be measured using a variety of techniques.

There are a number of sub-categories of ToF spectrometry, usually separated into mechanical and electronic gating methods. The former is termed *mechanical* because the neutron spectrum is made quasi-monochromatic in a controlled, mechanical manner and then measured. The method by which the spectrum is molded usually involves diffracting crystals or absorptive materials that bend or shunt the beam. On the other hand, electronically-gated methods do not use diffraction or absorption to remove sections of the spectrum, but instead use a variety of electronic deconvolution techniques.

In a mechanical Fermi chopper, an example of which is illustrated in Figure 7, neutrons impinge on one or more *monochromators*. These monochromators are crystals that use Bragg scattering to send those neutrons with wavelength λ_0 on the paths displayed in Figure 7 via the equation

$$\lambda_0 = 2d_M sin\theta_M, \tag{3}$$

where d_M is the spacing between reflecting planes in the monochromator, and θ_M is

16
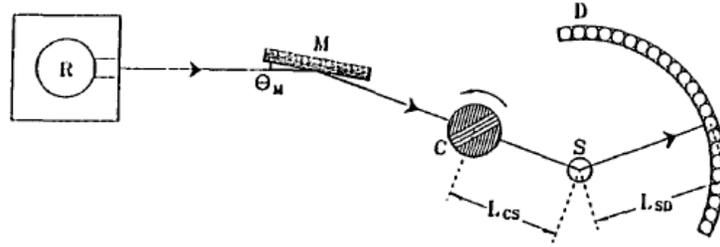
Figure 7. The schematic shows an example of a Time-of-Flight measurement set-up; R designates reactor or neutron source, M is the monochromator, C is the chopper, S is the sample or target, and D is the detector; θ_M is the monochromator diffracting angle, L_{CS} is the distance between the chopper and sample, and L_{SD} is the distance between the sample and detector.

the monochromator angle. The remaining neutrons travel through the Fermi chopper, C in the figure, which is essentially a spinning drum with slats that only allow through neutrons of the desired energy. These neutrons travel a distance, L_{CS} in Figure 7, before striking a target and scattering into the detector array, a distance of L_{SD} away from the target, where they are counted. The distances are known, so neutron energy ranges can be calculated based on the speed of the spinning drum.

A disk chopper, shown in Figure 8, removes neutrons of undesirable energies via absorption in the disk material. The advantages of this type of neutron spectrometer are its relative simplicity and the high beam intensity at the target position. However, it is limited by engineering constraints, as the disks rotate around 20,000 rpm. Thus, the disks must be very thin, typically on the order of 0.5-8 mm [7]. Therefore, the disk chopper is relevant for thermal neutron beams, but higher energy neutrons are not significantly attenuated by the disks and cause unwanted pulses in the detector [17].

There are a wide variety of electronic-chopping techniques; one studied was capture-gated spectrometry. In this method, a fast neutron interacts in a scintillator, produc-
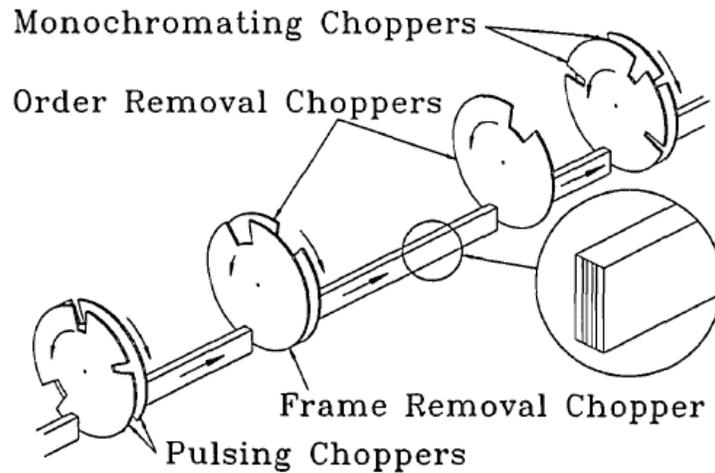
Figure 8. Another example of a mechanical chopper is the 4-point disk chopper shown here.

ing a pulse as a result of the energy transferred by the neutron in multiple-scatter events in the scintillator [19]. The experimenter cannot resolve these interactions, but bins them into a single scatter pulse. After an amount of time corresponding to the mean capture lifetime of neutrons in the material, a second capture pulse is observed. The amplitude of this capture pulse is equal to the Q-value of the neutron capture reaction. Using a deconvolution methodology similar to Bonner sphere spectrometry, the neutron energy spectrum can be obtained.

Mechanical ToF gating was not used for measurement of the IU NREP beam line due to the intensity of high-energy neutrons in the expected spectrum. Electronic capture-gating also was not chosen due to the complexity of the design, as compared to multiple-element neutron activation analysis. ToF also was not chosen, in general, due to uncertainty about the amount of physical space that could be used for a flight tube. Longer flight tube lengths provide increased spectrum energy resolution.

2.2.5 Fission Chamber

A fission chamber is based on the main principle of ionization chambers, with a slight twist. Instead of the interior being painted with an ionizing medium, the fission chamber is painted with fissionable material. Depending on the spectral response desired, an experimenter could use ^{235}U, ^{238}U, ^{239}Pu, or ^{232}Th [8]. In most situations, the material in fission chambers is in the form of a thin oxide coating, between 0.03 and 0.7 $\frac{mg}{cm^2}$ thick, on a metal foil [22]. The thicker the coating, the higher the efficiency of the detector. However, as thickness increases, the pulse height spectrum is skewed to lower energy because fission fragments lose energy while emerging from the fissile material. This coating may be painted, evaporated, electro-deposited, or sputtered onto the interior of the chamber. A diagram of a representative fission chamber system is shown in Figure 9.
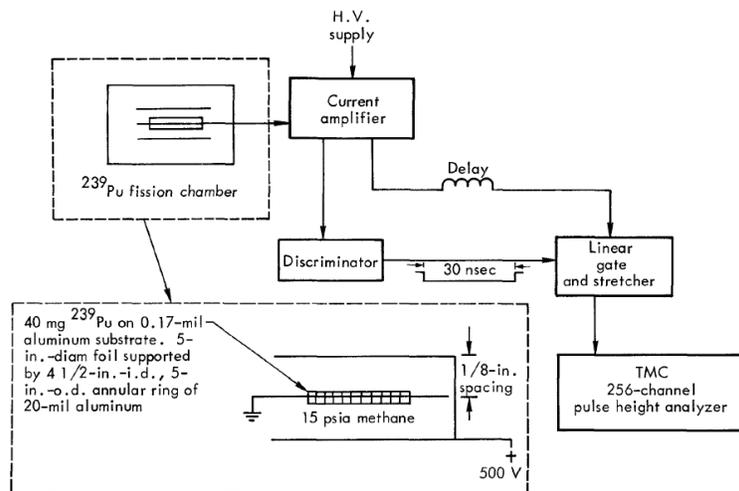
Figure 9. The schematic drawing of a fission chamber and associated electronic components shows an example of the components needed for analyzing the resultant spectrum.

Fission chambers are relatively simple, well-known devices. Their advantages include many years of study, as well as a clear separation of fission fragments from

19

alpha particle pileup. A major disadvantage is the necessity of the experimental facility to have a license from the Nuclear Regulatory Commission allowing the storage and use of radioisotopes. Also, because the fissionable material is thin to minimize fission fragment energy loss, efficiencies are typically low (often near 0.05%) [42].

Fission chambers were not used measure the neutron energy spectrum in this work. However, because the beam tripped off and the logging system was not adequate, a ^{235}U fission chamber was used to determine beam timing within 1.0 ($\pm$0.1) second. This is explained in further detail in Section 4.3.

2.3 Multiple-element Neutron Activation Analysis

The experimental method that was chosen to provide a basis for comparison to the simulation was multiple foil neutron activation analysis. It is a method of determining the incident neutron energy based on a known neutron capture reaction. Neutrons incident on a single-element thin foil or wire have a cross section for capture by the nuclei, creating a new species that may be radioactive. If the new species is radioactive, it decays with a characteristic half-life, and these decay products can be measured using techniques such as gamma ray spectroscopy. The half-life of a material is the amount of time it takes for half the radioactive atoms present in the material to decay to a different isotope, leaving half of the original activity.

In the simplest situation, the thin foil does not significantly disturb the neutron flux, so the rate of change in the number of radioactive nuclei, $\frac{dN}{dt}$, can be described by

$$\frac{dN}{dt} = R - \lambda N, \tag{4}$$

where R is the rate of formation, λ is the decay constant, and N is the number of

20

radioactive nuclei present. The rate of formation is given by

$$R = \phi(E)\Sigma_{act}(E)V, \tag{5}$$

where $\phi(E)$ and $\Sigma_{act}(E)$ are the energy-dependent neutron flux and activation cross section, respectively, and V is the foil/wire volume. Equation 4 can be solved, assuming R is constant and $N(t = 0) = 0$, as

$$N(t) = \frac{R}{\lambda}\left(1 - e^{-\lambda t}\right). \tag{6}$$

However, knowing that the activity, A(t), is equal to the product of λ and N(t), Equation 6 becomes

$$A(t) = R\left(1 - e^{-\lambda t}\right). \tag{7}$$

The resultant activity is indicative of the incident neutron flux, and the activity is used in unfolding the neutron spectrum by using threshold detectors and cadmium covers. These concepts are discussed in Sections 2.3.1 and 2.3.2. However, to properly unfold a neutron spectrum, the reaction rate must be measured at saturation. This will be further discussed in Section 2.3.3.

2.3.1 Threshold Activation Detectors

There are two types of materials used for neutron activation analysis: *whole-spectrum* and *threshold* detectors. The basic principle considers the *Q-value*, or the decay energy, of a reaction. The Q-value is defined as [24]

$$Q = \left(m_{initial} - m_{final}\right)c^2$$
$$= \left(m_X + m_a - m_Y - m_b\right)c^2, \tag{8}$$

21

where m is the atomic mass, X designates the target atom, Y is the resultant atom, a is the incident particle, and b is the by-product. If $Q < 0$, energy must be input for the reaction to occur, and the reaction is called *endoergic*. Conversely, for $Q > 0$, energy is released, and the reaction is *exoergic*.

Whole-spectrum detectors are characterized by reactions that can theoretically occur using neutrons with zero energy because the Q-value is ≥ 0. Thus, the reaction rate is only limited by the reaction cross-section, which is energy-dependent. Gold has an isotope that falls into this category. Its relevant reaction, $^{197}Au(n, \gamma)^{198}Au$, has a Q-value of 6.51239 MeV [34] and thus the reaction is exoergic. The excess energy contributes to the kinetic energy of the products.

Threshold detectors, on the other hand, are neutron activation foils/wires that are of isotopes whose neutron-absorptive reactions require energy to occur. One such isotope is ^{27}Al. Natural aluminum, which contains 100% ^{27}Al, can absorb a neutron to create ^{27}Mg or ^{24}Na via the reactions, $^{27}Al(n, p)^{27}Mg$ and $^{27}Al(n, \alpha)^{24}Na$. These two reactions have negative Q-values, -1.82799 MeV and -3.13284 MeV respectively, making them endoergic. Therefore, the reactant system must contain enough kinetic energy to overcome this threshold. The required kinetic energy can be described [24] by

$$KE_{th} = -Q \frac{m_Y + m_b}{m_Y + m_b - m_a}, \tag{9}$$

where Q is the Q-value.

Both whole-spectrum and threshold detectors are used in neutron activation analysis to accomplish spectrum unfolding as they both provide reference points for understanding the energy dependence of the system. In combination with cadmium covers, they help to more accurately map the neutron energy spectrum.

2.3.2 Cadmium Covers

Cadmium covers are used in neutron activation analysis experiments because of cadmium's strong neutron absorptive property. This is also energy dependent and is better understood when considering the energy-dependent cross-section for absorption for natural cadmium, plotted in Figure 10. The cross section is highest from very low energies to approximately 0.5 eV, which is called the *cut-off* region. While there are some resonances from 1 eV to 10 keV with appreciable cross sections, the integrated cross section is much smaller. This gives rise to a correction factor used when calculating the thermal flux. In essence, almost all thermal neutrons, those below about 0.5 eV, are absorbed in the cadmium cover while higher energy neutrons have a high probability of penetrating the cadmium cover to reach the material inside.
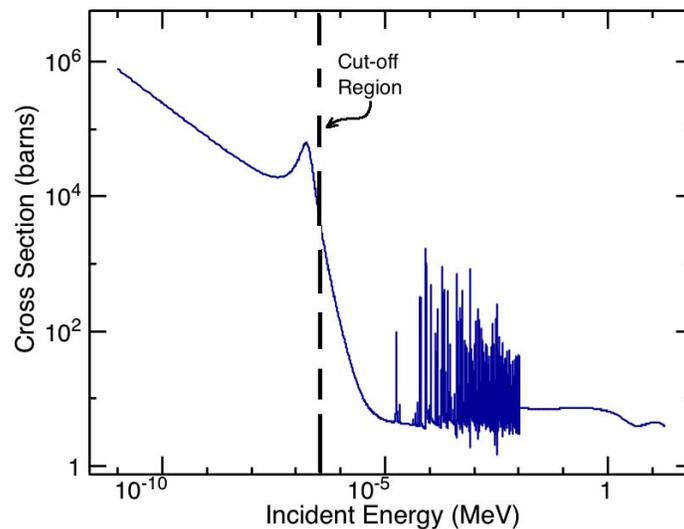
Figure 10. The cross section for ^{113}Cd as a function of incident neutron energy provides an understanding of the likelihood of interaction at various energies.

In this research, cadmium covers were used to provide the SAND-II unfolding algorithm more data points by which unfolding can be accomplished. By using cad-

23

mium covers during irradiation, most of the neutrons with energy less than 0.5 eV are absorbed and cannot induce activity in the sample. Effectively, this creates an "artificial threshold" reaction. The SAND-II code was created with the ability to include cadmium absorber in its unfolding technique, so no modifications were needed.

When calculating thermal flux using cadmium covers, the equation for the activity induced in the material due to the thermal flux is

$$A_{th} = A_m - F_{Cd}A_{Cd}, \tag{10}$$

where A_m is the measured activity for bare foils, F_{Cd} is the cadmium correction factor, and A_{Cd} is the measured activity with Cd covers. Since cadmium effectively absorbs thermal neutrons, energy dependence is removed from the reaction rate equation. In essence the reaction rate, R becomes

$$R = \phi_{th}\Sigma_{act}^{th}V. \tag{11}$$

where ϕ_{th} is the thermal neutron flux and Σ_{act}^{th} is the macroscopic thermal neutron activation cross section. Equation 10 can be arranged to solve for the thermal flux,

$$\phi_{th} = \frac{R}{\Sigma_{act}^{th}V}, \tag{12}$$

which can subsequently be solved to yield the thermal flux. The macroscopic cross section for activation can be described by

$$\Sigma_{act}^{th} = \sigma_{act}^{th}N, \tag{13}$$

where σ_{act}^{th} is the microscopic thermal neutron activation cross section and $N = \frac{\rho N_a}{M}$. In this case, ρ is the foil/wire material density, N_a is Avagadro's number

24

$\left(6.022x10^{23}\frac{atoms}{mole}\right)$, and M is the atomic mass in grams/mole.

2.3.3 Saturation Level & Correction

If the foil is left in the neutron flux environment long enough, the activity reaches a saturation level as described by $A_\infty = R$. Knoll [22] has defined the amount of time a sample must be irradiated to be activated sufficiently close to saturation to be equal to 3-4 half lives, which approaches 88–94% of the saturation activity. However, with a pulsed beam, one hour of beam operation is equivalent to approximately 30 seconds of total irradiation time for the observed beam duty factor of 0.9%. The shortest lived daughter product created in the experiments, ^{24}Na, has a half-life of 564 seconds. The amount of beam time required to meet the saturation requirement would be over 50 hours of continuous beam operation, while the maximum beam time that could be obtained during the experiments was approximately 3 hours due to operational constraints of the LINAC power supply. Obviously, irradiation to saturation was not possible for any of the materials being irradiated.
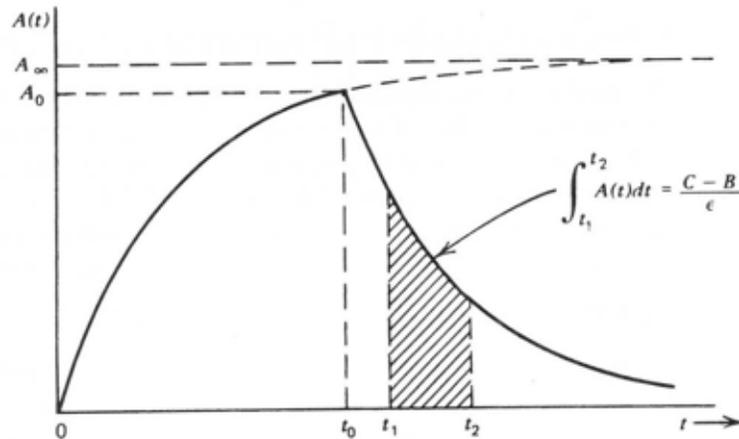
Figure 11. The activity of an irradiated foil is shown as a function of time, where A_∞ is the saturation activity, A_0 is the activity at the end of irradiation, t_0 is the end irradiation time, t_1 is the start count time, and t_2 is the end count time.

25

A correction can be made [22], and this is described as the activity at infinite time, A_∞. To solve for this value, a scenario is constructed by which activity is built up and then decays. The activity as a function of time, $A(t)$, is displayed in Figure 11. A sample is irradiated for a time, t_0. Activity builds according to Equation 7 until it reaches A_0 at t_0. At this point irradiation ends, and the activity decreases due to radioactive decay as a function of the half life. At time t_1, counting is begun. Finally, counting ends at time t_2. The total number of counts measured is described by

$$C = \epsilon \int_{t_1}^{t_2} A_0 e^{-\lambda(t-t_0)} \, \mathrm{d}t + B \tag{14}$$

$$= \epsilon \left(\frac{A_0}{\lambda} \right) e^{\lambda t_0} \left(e^{-\lambda t_1} - e^{-\lambda t_2} \right) + B. \tag{15}$$

where C is the number of counts measured in the counting interval, B is the background counts, and ϵ is the detector efficiency. Rearranging Equation 15 for A_0 and knowing that $A_0 = A_\infty \left(1 - e^{-\lambda t_0} \right)$, the activity at infinity is described as

$$A_\infty = \frac{\lambda(C - B)}{\epsilon \left(1 - e^{-\lambda t_0} \right) e^{\lambda t_0} \left(e^{-\lambda t_1} - e^{-\lambda t_2} \right)}. \tag{16}$$

2.3.4 SAND-II Computer Code

The Spectrum Analysis for Neutron Detectors, Ver 2 (SAND-II) computer program was developed at Sandia National Laboratory (SNL) as an automated, nonlinear, least squares, iterative perturbation method to deconvolve the neutron flux spectrum based on an initial guess, provided by the user. The initial guess suggests *a priori* knowledge of the spectrum, which is where modeling and simulation are applied.

The steps to calculation are as follows. First, the code calculates the expected activity in a material based on the user's initial guess of the neutron energy spectrum

as well as the bulk material cross-sections. Next, an activity weight function, ω is calculated for each energy bin,

$$\omega_{i,j}^k = \frac{1}{2}\frac{A_{i,j}^k + A_{i,j-1}^k}{A_i^k}, \ j = 2,\ldots,m. \tag{17}$$

In Equation 17, A is the activity, i is the foil material index, j is the energy bin index, k is the iteration index, and m is the total number of energy bins. After calculating this weighting function, the ratio of measured to calculated activities is computed as R_i^k and it is applied to derive a correction factor, c_j^k, for each energy bin

$$c_j^k \ = \ \frac{\displaystyle\sum_{i=1}^n \left(\omega_{i,j}^k \ln\left[R_i^k\right]\right)}{\displaystyle\sum_{i=1}^n \omega_{i,j}^k}, \tag{18}$$

where n is the number of foils used in the deconvolution. To yield the next iteration's flux value, ϕ_j^{k+1}, this correction factor is applied to the flux value for every energy bin, ϕ_j^k, by

$$\phi_j^{k+1} = \phi_j^k e^{c_j^k}. \tag{19}$$

This process is continued until the user-defined solution criteria are met or a maximum number of iterations is reached, as described further below. The details of the mathematical modelling can be found in Berg and McElroy's manual for the program [30]. However, a few points must be made regarding its usage.

First, the code was developed for the express purpose of determining the spectrum and absolute magnitude of a neutron environment from the activity induced in activation samples. It starts from a "guess" spectrum defined by the user. This presupposes that the user has some idea of the spectrum. In the case of this research, two initial spectra were used: one was derived from MCNP simulations done

27

by IU personnel in the past, and the other based on a GEANT model of the neutron production spectrum, which will be discussed further in Section 3.3.

Another point of distinction with the SAND-II code is that it assumes that all input activity measurements are already adjusted to infinite dilution. In essence, the code does not automatically correct for the effects of self-shielding or not reaching saturation. Therefore, these calculations, as discussed in Section 2.3.3, must be done prior to running the SAND-II code.

In addition, the SAND-II code was built with the capability to include flux attenuation by foil cover materials like cadmium and boron. It includes the total cadmium cross sections as well as the boron neutron capture cross sections $[^{10}B(n, \alpha)^{7}Li]$ and gives the user the ability to define the cover species and thickness.

Another user input property is the acceptable solution criterion. After each iteration, a "deviation" parameter is calculated [43]. The equation for this parameter is

$$DEV = S = \left[\frac{1}{n-1} \sum_{i=1}^{n} \left(\frac{A_i^m}{A_i^c} - 1 \right) \right]^{\frac{1}{2}}, \tag{20}$$

where A_i^c designates calculated activities, A_i^m designates measured activities and n is the number of foils. Once DEV reaches an acceptable value, typically 5-10%, the iteration ceases and the solution is considered valid. Additionally, if the calculated deviation parameter becomes stable to within less than a one percent change per iteration without reaching the user-defined acceptable value, iteration stops and a warning message is included in the output file.

Once iteration is completed, either by convergence or by termination, the spectrum is output. SAND-II uses a discrete energy interval model rather than a continuous model. There are 620 energy intervals between 10^{-10} and 18 MeV broken up in the following manner: from 10^{-10} to 1 MeV, there are 45 intervals per decade resulting

28

in a bin size in the first decade from 10^{-10} to 10^{-9} of 5×10^{-12} MeV; then, there are 170 intervals from 1 MeV to 18 MeV, thus the increments are 0.1 MeV per bin. The spectrum that is output is tabulated at the upper and lower bounds of each interval giving a total of 621 points.

2.4   Monte Carlo & GEANT

GEometry ANd Tracking (GEANT) is a Monte Carlo computer code developed for high-energy physics applications at Conseil Européen pour la Recherche Nucléaire (CERN) [5]. GEANT, currently in its 4th generation, is a toolkit written in C^{++} that allows users to model the transport and interaction of particles with matter. Historically, its treatment of low-energy phenomena has been minimal. In recent years, new modules have been written to more accurately model low-energy physics interactions.

2.4.1   GEANT Variable Selection Method

As stated in the GEANT physics reference manual [40], the toolkit mixes the composition and rejection Monte Carlo methods. Rubinstein and Kroese [37] describe composition as a method by which a sample can be selected from a cumulative distribution function (CDF), F, assuming it can be described by a collection of CDFs, G_i:

$$F(x) = \sum_{i=1}^{m} p_i G_i(x), \tag{21}$$

where m is the total number of CDFs, $p_i > 0$ is a probability and the sum of all p_i's is 1. A random variable is then generated from this composition of CDFs. This method is considered a *direct* method in that it deals directly with the variable to be generated.

29

On the other hand, the rejection method (sometimes known as the *acceptance-rejection* method) is an indirect method developed by two of the creators of the Monte Carlo technique, Stanislaw Ulam and John von Neumann [37]. The algorithm has three steps. Consider a probability density function (PDF), $f(x)$ as shown in Figure 12. The x-axis represents the independent variable, and the y-axis is the dependent variable to be chosen. In this case, a and b are the lower and upper bounds of the dependent variable, respectively, and c is the maximum value of the function, $f(x)$. The first step is to generate an x value between a and b. This value of x provides the acceptance/rejection criterion. Next, a random value for y is selected independently from the value of x; it must be between 0 and c. Finally, x is accepted if y is $\leq f(x)$. If not, it is rejected, the algorithm returns to step 1, and the process is repeated until an acceptable value is found.
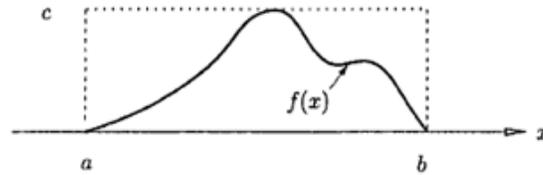
Figure 12. The acceptance-rejection method of Monte Carlo simulation uses a sample set (dotted line) surrounding the probability density function and rejects any values greater than the function value, $f(x)$.

2.4.2   Simulation Steps

The GEANT toolkit transports each particle from its generation point to the point at which it stops, is absorbed, or leaves the simulation space. It then simulates the transport of the next particle. Via the randomization techniques described in Section 2.4.1, the probability and location of interaction are selected. The GEANT

30

toolkit monitors a particle's path through a material in increments called *steps*. First, the cross-section and mean free path of the current particle are calculated for the material through which the particle is traveling. Cross-section, the probability that a particular interaction will occur in the material, can be determined by selecting values from a parametrized table, which is the most likely case at energies ≥ 20 MeV, or by applying a low energy theoretical model. The mean free path, λ, is then calculated as:

$$\lambda\left(E\right) = \left(\sum_i n_{ati} \cdot \sigma\left(Z_i, E\right)\right)^{-1}, \tag{22}$$

where n_{ati} is the number of atoms per unit volume of the ith element of the material, Z_i is the atomic number of the ith element, and σ is the microscopic cross section of the Z_i^{th} element at the particular energy E for the interaction of interest. Because the cross-section and mean free path are discontinuous in a volume, both must be calculated at each simulation step. If no interaction occurs, the particle is transported to the next step's starting point, and the process is repeated.

The GEANT toolkit defines a *hit* as an interaction of a particle in a material, and the GEANT simulation process must then determine the end state for the interaction participants. Variables calculated for each interaction include, but are not limited to, the energy deposited by the incident particle, the final state vector of the particle, the spatial distribution of the deposited energy throughout the interaction medium, and the properties of any secondary particles created.

31

III. Simulation

In order to better understand the NREP neutron environment and provide an initial guess for input into the SAND-II unfolding code, simulations utilizing the MCNP and GEANT software packages were completed. In the former case, input decks were obtained from Dr. Charles Lavelle [26] and Dr. Sangjin Lee [27]; for the latter, the geometry was built using the dimensions found in the MCNP input decks. In the following sections, the geometry will be described, a comparison between the MCNP and GEANT cases will be made, the simulation method will be discussed, and the simulation results presented.

3.1 Geometry Definition

It is possible for simulation codes such as GEANT to incorporate as much geometric complexity as the user desires. However, increased complexity requires additional computing resources. In the course of this research, two levels of complexity were considered and simulated: a simple, low fidelity geometry in GEANT, as well as one that was more complex with higher fidelity in both GEANT and MCNP. The physics models applied to the simple geometry scenario were identical to those applied to the complex geometry scenario. The former was the only geometry that could be simulated successfully in GEANT; the consequences of this will be discussed in Section 3.1.2.

3.1.1 Simple Geometry (GEANT)

This simulation environment consisted of a simple geometry to verify the validity of the physics processes and threshold cuts selected, while also quantifying a neutron "birth spectrum". The birth energy spectrum of neutrons generated via the ^{9}Be(p,n)

reaction has been reported in literature for proton energies lower than 5 MeV [18] and higher than 17 MeV ([6], [12]). However, there is no experimental information about the neutron production spectrum in the energy range of the protons at the IU LINAC (7-13 MeV), therefore it is not possible to do a quantitative comparison with experimental literature. However, in the study of the LENS TMR [25], calculations were performed based on fundamental nuclear physics principles to predict the expected neutron birth energy spectrum. Figure 13 shows both bounding experimental works as well as the calculations from [25]. By measuring the birth spectrum of the neutrons in the simple GEANT scenario, a comparison can be made between the GEANT model and calculations.
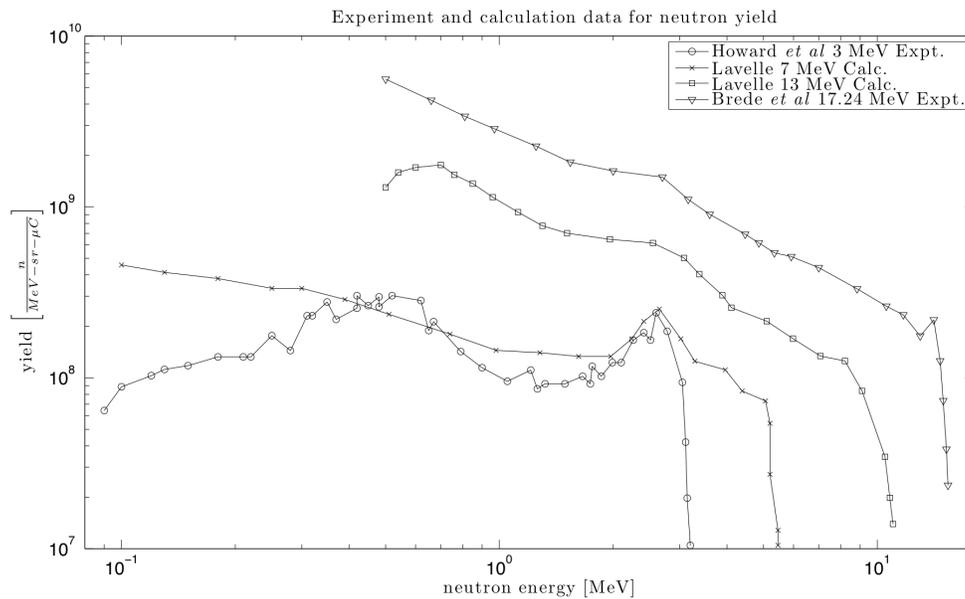
Figure 13. The birth energy spectrum of the neutrons as a function of incident proton energy from literature for both experiment and calculation; the data plotted from Lavelle [25] is calculated, while data from Howard *et al.* [18] and Brede *et al.* [12] are experimental.

The simple geometry contained four relevant aspects. First, the protons incident on the target possessed an initial energy of 13 MeV. Next, the beam line was $10 \times 10 \times 50$ cm and made from 0.5 cm thick natural aluminum containing air at $7.5x10^{-5}$ torr to simulate vacuum. Within this vacuum, a 0.15 cm radius sphere of natural beryllium (100% ^{9}Be) was placed at the geometrical center of the beam line. The radius of the sphere was selected as 0.15 cm so that all protons stop within the sphere, but the likelihood of neutron scattering interactions in the beryllium is low.
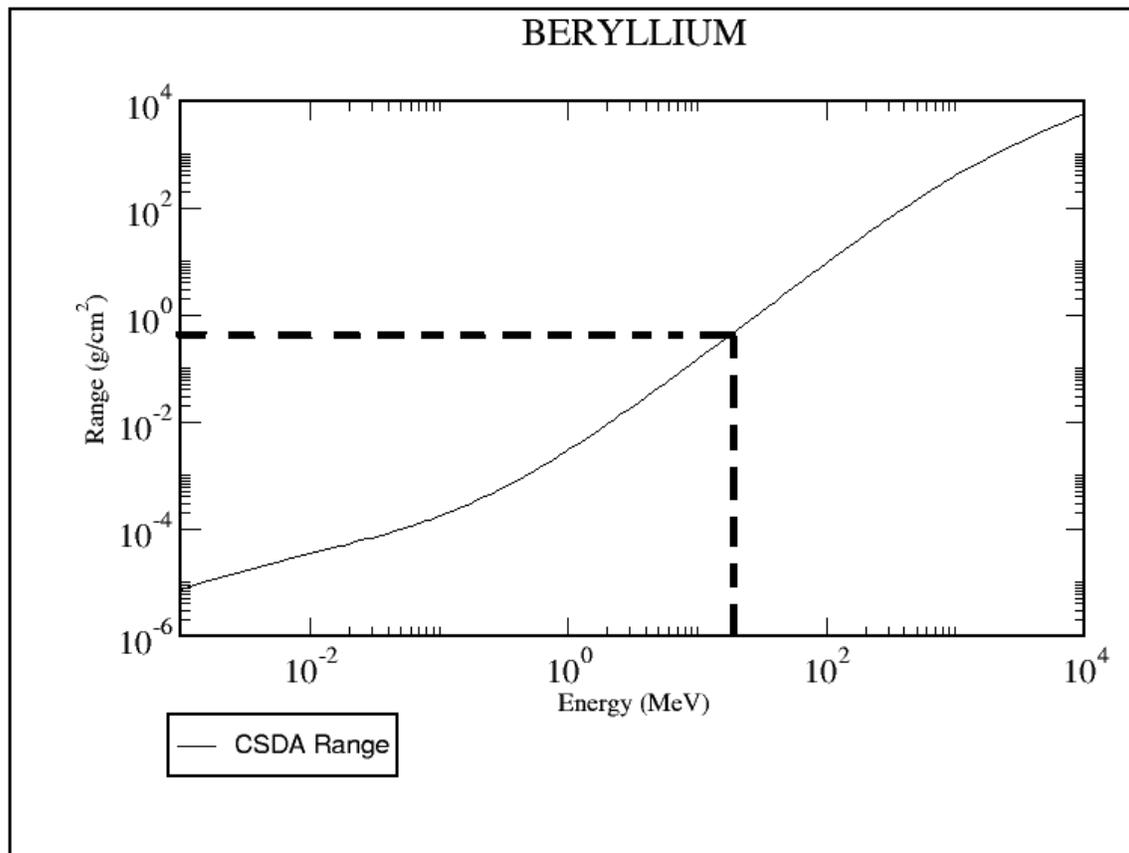
Figure 14. **The x-axis describes incident proton energy in MeV while the y-axis is the proton range in $\frac{g}{cm^2}$; the range of protons in beryllium for 13 MeV protons is $2.375x10^{-1}\frac{g}{cm^2}$ using the Continuous Slowing Down Approximation (CSDA) method.**

34

To make this statement, the concept of range is introduced. Range is a measure of the average path length travelled by a charged particle as it slows down via scattering. Range is calculated using the *Continuous Slowing Down Approximation* (CSDA) method in which the rate of energy loss at every point along the track is assumed to be equal to the total stopping power. Stopping power is the average energy loss of the particle per unit path length. Figure 14 displays the range of protons in beryllium in units of $\frac{g}{cm^2}$. The range of 13 MeV protons in beryllium is $2.375 x 10^{-1} \frac{g}{cm^2}$. If the density of Be ρ_{Be} is $1.85 \frac{g}{cm^3}$, the range is 0.128 cm.
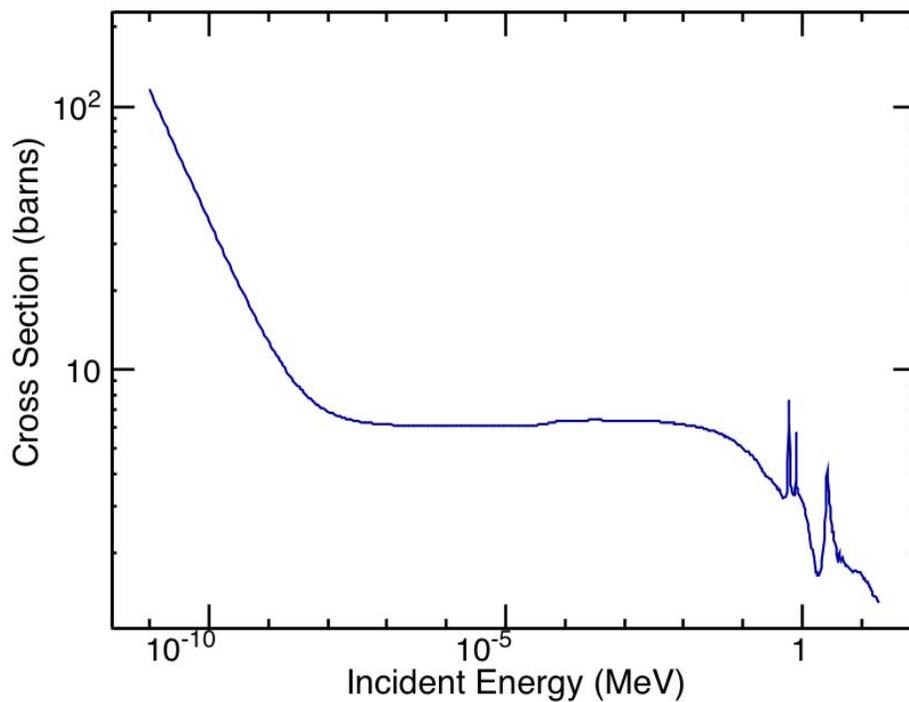
Figure 15. The total microscopic cross section for neutrons in beryllium is plotted as a function of neutron energy in MeV.

Mean free path, λ, is defined as the average distance a particle travels before a particular interaction occurs. It is defined as $\lambda = [\Sigma_i]^{-1}$ where Σ_i is the macroscopic

35

cross section for the particular reaction, or $\Sigma_i = N\sigma_i$ where σ_i is the microscopic cross section. N, the number density, is defined as $N = \frac{\rho N_a}{M}$ where ρ is the material density, N_a is Avagadro's number $\left(6.022x10^{23}\frac{atoms}{mole}\right)$, and M is the atomic weight of the material in $\frac{g}{mole}$. For beryllium with $\rho = 1.85\frac{g}{cm^3}$ and $M = 9.012182\frac{g}{mole}$, the number density is $1.236x10^{23}cm^{-3}$.

The total microscopic cross section for neutrons in beryllium is plotted in Figure 15, which comes from the Evaluated Nuclear Data File B, Version 7.0 (ENDF/B-VII.0) [1]. For neutrons of thermal (0.025 eV) through most of the epithermal energy range (<0.1 MeV), the cross section is approximately 7.5 barns. Past 0.1 MeV, the cross section drops, albeit with some resonances. As such, the macroscopic cross section can be approximated, since 1 barn = 10^{-24} cm^2, as 0.95 cm^{-1}. For this reason, the mean free path is 1.05 cm. Considering that the maximum distance that a neutron could travel before exiting the sphere without interacting is the diameter of the sphere or 0.3 cm, the probability of the neutron interacting inside the beryllium is small. Thus, the neutron will most likely not interact before leaving the sphere.

The final aspect of the simple geometry design was a 4.5 cm radius sphere, whose origin was the same as that of the beryllium sphere and that was made of the same vacuum as the beam line. It was used as a monitor to determine the neutron creation angle for analysis of the birth momentum direction discussed in Section 3.3.2.3. This was accomplished by producing an output whenever neutrons stepped into the spherical monitor's volume. This output contained the neutron's location and kinetic energy as well as its birth location and birth kinetic energy. Figure 16 shows a schematic of this set-up using GEANT visualization software (HepRApp). The results of this simulation will be discussed in Section 3.3.

www.manaraa.com
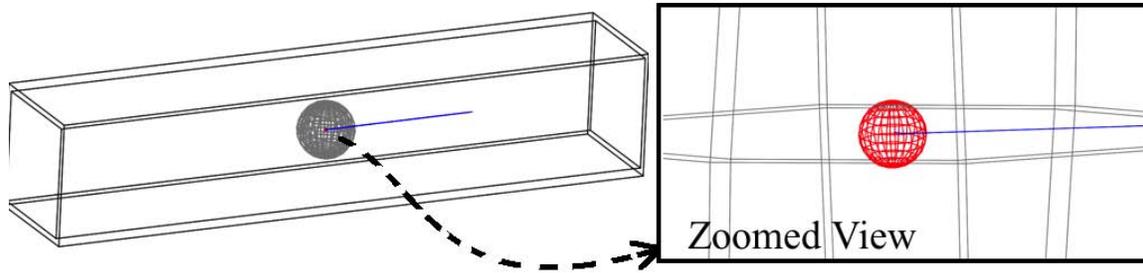
Figure 16. The schematic of the simple GEANT geometry displays the system in the figure on the right: the beam line is the black rectangular prism, the beryllium target is red, the spherical sensitive detector is grey, and the incoming proton (traveling right to left) is dark blue; the image on the right is zoomed in to show the proton impacting the beryllium sphere.

3.1.2   Complex Geometry (GEANT/MCNP)

While the simple geometry is helpful in verifying the physics and making sure the code compiles, it makes many assumptions and simplifications that may compromise the physical reality of the situation. To increase fidelity in the simulation, a more complex geometry must be built that removes many of these simplifications. To this end, an environment was built using the GEANT geometry toolkit using the geometric parameters found in the MCNP input deck created by Lavelle [25].

3.1.3   GEANT Complex Geometry Definition

Table 1 displays the materials used in the complex geometry simulation, and the numbers correspond to the property definitions found in Table 2. The scenario for the complex geometry included an aluminum beam line through which 13 MeV protons pass to reach the beryllium target. The target assembly was at the terminus of the beam line and was a 10.48×16.65 cm rectangle, with a thickness of 0.40 cm. The beryllium target was made of natural beryllium (100% ^{9}Be). It was contained in a 13.97×20.32×5.1275 cm aluminum box with a 1.19 cm thick coolant water channel on the downstream face. This beam line and target assembly terminated in a Target-

37

Moderator-Reflector (TMR) made out of nested cylinders of various neutron and gamma absorbing materials. For instance, the outermost shell was 2.7 m high with a radius of 1.07 m and was made from borated polyethylene containing a 2.142% Mass Fraction (MF) of boron. The other shells included a lead gamma shield, a 30% borated polyethylene neutron decoupler layer, and a 0.24% borated lead brick layer.

Table 1. Descriptions of the materials defined in Table 2.

#	Name	Description
1	2.142% Borated PE	Polyethylene used in outer TMR shell
2	Air	Defined at standard temperature and pressure
3	Water	Coolant for beryllium target
4	Methane	Moderator, not used for NREP sim. geometry
5	Aluminum	6061 structural aluminum alloy for beam line
6	0.24% Borated Lead	Bricks used for additional shielding
7	30% Borated PE	Polyethylene layer for inner decoupling
8	Beam line vacuum	Same as air, pressure $= 7.5 \times 10^{-5}$ torr
9	Lead	Inner TMR gamma shield
10	Be target	Beryllium target material
11	Pure PE	Used as filler in many places

Table 2. Material properties for complex geometry file definition; MF = Mass Fraction, E = Element.

$\#^1$	ρ [g/cm^3]	E	MF [%]	E	MF [%]	E	MF [%]	E	MF [%]
1	0.96700	H	65.24	C	32.62	B	2.14		
2	0.00129	N	70	O	30				
3	1.00000	H	66.67	O	33.33				
4	0.46600	H	80	C	20				
5	2.70000	Al	100						
6	7.38000	Pb	92.31	C	6.41	H	1.07	B	0.22
7	1.65000	H	58.1	C	29.12	B	12.86		
8	$1.27x10^{-10}$	N	70	O	30				
9	11.34000	Pb	100						
10	1.85000	^{9}Be	100						
11	0.92000	H	66.7	C	33				
^{1}Material numbers defined in Table 1									

38

Also included in the geometry was the apparatus for containing the cryogenic methane neutron moderator, which consisted of aluminum components capable of vacuum-sealing. This entire geometry was contained within a 6×6×6 m cube experimental hall filled with air at standard temperature and pressure. The beam line's vacuum was made from the same air, but it was set at a pressure equal to 7.5×10^{-5} torr.

This GEANT geometry was built using the parameters described in the MCNP input deck of [25]. However, as the geometry was being built and tested, a problem arose that stopped work. Despite attempting to recess the end of the beam line in the TMR, the beam line vacuum terminates at the outer TMR shell. The incident protons cannot reach the target because they are stopped by the outer borated polyethylene cylinder. Work to fix this issue has continued; unfortunately, it was not corrected in time to be used in this research. For this reason, results of this simulation were not used in the input spectrum for SAND-II, and the MCNP model from [25] was used. The MCNP model is discussed in Section 3.1.4.

3.1.4   MCNP Model

Monte Carlo N-Particle (MCNP) is a particle transport simulation code created by scientists at SNL. The original purpose of the code was to determine criticality in nuclear experiments. However, it has been modified over the years to model more processes and particles of interest to radiation transport. It differs from GEANT in that it has little flexibility in physics models: an input deck provides geometry, material, and particle descriptions, while cross-section libraries provide probabilities for the various interaction processes.

The models in ([26], [27]) simulate the LENS TMR. Unfortunately, this is a different beam line, and a major difference is the presence of a moderator between the

39

beryllium target and the location of irradiated samples. In the model of the LENS TMR, a liquid methane region moderates neutrons. Methane, CH_4, has a significant cross section for scattering, which absorbs a significant amount of energy from the neutrons as they travel through the moderator region. Therefore, the energy spectrum of the neutrons that emerge is shifted to lower energies. In the NREP TMR, the methane moderator and its constituent apparatus for holding it at cryogenic temperatures is replaced by an air void with significantly less moderating capability. For this reason, one would expect that the spectrum observed in the NREP would be closer to the $^9Be(p,n)$ neutron birth spectrum, as compared with the spectrum observed at the LENS.

Another difference between the GEANT model and the MCNP model is the MCNP model does not simulate the production of neutrons. The particle source term for MCNP5 is limited to neutrons or gammas. Therefore, a neutron production term from an incident proton beam must be derived. An energy probability distribution of neutrons was calculated based on experimental literature [25]. An angular-dependent energy probability density for the neutrons was then calculated, as displayed on the left in Figure 17, which was used as a user-defined table in the MCNP input deck. The results of the simulation produced a spectrum, displayed in the right plot in Figure 17, that was used as the input spectrum for the SAND-II spectrum unfolding code.

3.2 Physics List Selection

The critical advantage of GEANT over other Monte Carlo transport codes is its ability to allow the user to select from a variety of physical processes and interactions. In this way, GEANT allows significant customization of the code environment, which can reduce the required computational resources while producing physically accurate

40
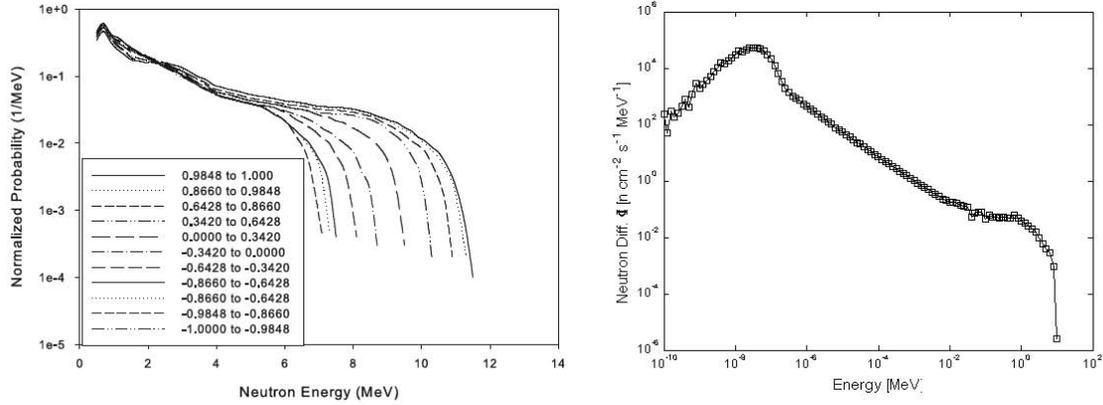
Figure 17. <u>Left:</u> The energy probability distribution used in MCNP input for $E_p = 13$ MeV at each angle, as calculated by IU personnel[25]. <u>Right:</u> The neutron flux spectrum at a plane 2 cm from the back face of the beryllium target provided one of the input guess spectra for the SAND-II spectrum unfolding code.

results. The backbone of this customization method is the selection of a proper *physics list*, which is a module within the overall code structure that prompts the GEANT toolkit to utilize specified physics processes during simulation. Users can select from seven major process trees: Electromagnetic, Hadronic, Decay, Photolepton-Hadron, Optical, Parameterization, and Transportation. Each of these standard processes can be defined further. For example, the Electromagenetic tree can be split into photonic processes, electron/positron processes, and muon interactions, among others. Each of these can be segmented further. For example, the photonic process branch can be broken into Compton scattering, electronic pair production, photo-electric effect, and muon pair production [31].

It is up to the user to define which of these processes is important to his or her simulation. In this case, the physics list selected was broken into the particle types to be transported. Table 3 lists the processes used for the two primary particles of interest in the simulation.

Table 3. The primary two particle groups considered in the physics list for the NREP beam line simulation.

Uncharged Hadrons (Neutrons)	Charged Hadrons (Protons)
Elastic Scattering	Low Energy Ionization
Inelastic Scattering	Elastic Scattering
Capture	Inelastic Scattering
Fission	Multiple Scat.

3.2.1 Uncharged Hadron (Neutron) Physics

Neutron interaction physics is the primary interest of this research, and as such, the physics list is the most detailed. The processes included are inelastic and elastic scattering, capture, and fission. Since the scenario involves low-energy interactions, as defined by the GEANT code, the models used for each process include the low-energy counterparts developed in recent years. All cross section calculations use the Evaluated Nuclear Data Files, B version 6 (ENDF/B-VI) via implementation in the *G4NDL* neutron data libraries. This research used *G4NDL* version 3.13 [5].

The primary advantage of using these high-precision data models is the increased accuracy gained by utilizing the evaluated nuclear data libraries; however, this is very computationally intense. Also, the ENDF libraries are only valid for a particular energy range. Therefore, it is not always advantageous to use these models. For this reason, the high-precision models are only used in the energy intervals where they provide the greatest advantage.

3.2.1.1 Elastic/Inelastic Scattering processes

Neutron elastic scattering considers collision interactions in which total kinetic energy is conserved. Three different models are applied to neutrons of three energy bands. All neutrons above 19 MeV use the parametric-based elastic scattering model implemented via the *G4LElastic* class. Neutrons below 19 MeV, but above 4

42

eV, utilize the high precision neutron models set by the *G4NeutronHPElastic* class, which depend on the ENDF/B-VI libraries produced by the National Nuclear Data Center at Brookhaven Laboratories. Finally, thermal neutron scattering is treated by thermal scattering data tables generated from the ENDF/B-VI, utilized by the *G4NeutronHPThermalScattering* class.

Inelastic neutron scattering occurs when the incident neutron causes excitation of the target nucleus and leaves the collision with a different energy relative to its incident energy. In this case, two models were used. All neutrons above 19 MeV are governed by the *G4LENeutronInelastic* model for hadron inelastic scattering. Below 19 MeV, high precision models implemented in the *G4NeutronHPInelastic* class use the neutron data libraries.

3.2.1.2 Capture Processes

Neutron capture occurs when a nucleus combines with an incident neutron to form a compound nucleus, often in an excited state. To be considered a *capture reaction*, a process must produce a by-product that can reach a statistical, thermal equilibrium. Therefore, a reaction that produces a metastable by-product that decays in nanoseconds may not be considered a neutron capture, but an inelastic scattering event. On the other hand, if the by-product decays to ground state by gamma emission with a half life of 2.6 days such as the unstable ^{198}Au nucleus, this would be considered a capture process.

As in the elastic/inelastic scattering case, neutron capture is treated in two increments. Above 19 MeV, the *G4LCapture* class is implemented, while the high-precision low-energy models of *G4NeutronHPCapture* apply to neutrons lower than 19 MeV.

3.2.1.3   Induced Fission

Incident neutrons can also induce fission in various fissionable and fissile isotopes. As with the other neutron processes, the neutron energy spectrum is broken at 19 MeV, with the high energy parametrization models used above and the high precision ENDF/B-VI data tables used below. High energy parameterization is implemented using the *G4LFission* model, and low energy neutrons are treated using the *G4NeutronHPFission* class.

3.2.2   Charged Hadron (Proton) Physics

Proton interaction within beryllium is the mechanism by which neutrons are produced in this system. Protons were treated separately from generic ions in the physics list.

3.2.2.1   Low-Energy Ionization

Low energy ionization was implemented using the *G4hLowEnergyIonisation* class, and a number of secondary settings were turned on as well. The ICRU R49 electronic and nuclear stopping models, fluorescence, and Auger electron production were used. The stopping models describe how ions deposit their energy as they travel through a material. Fluorescence is the emission of light photons by a material that has absorbed energy, in this case due to energy deposition by the proton. Auger electrons are those that are ejected from an atom due to the energy emitted after an outer-shell electron drops into an inner-shell vacancy created by an incident ion.

3.2.2.2   Elastic and Inelastic Scattering

Elastic scattering in the material is treated using the *G4LElastic* class for all proton energies. On the other hand, the inelastic scattering of protons is implemented

44

using the *G4LEProtonInelastic* class for protons with energy less than 20 MeV.

3.2.2.3   Multiple Scattering

Multiple scattering events are considered a process common to all charged particles. Essentially, to save computational resources, the code uses multiple scattering tables generated from literature (e.g. [28], [16], [14]) to determine the probability of multiple scattering. On the other hand, single elastic scattering is advantageous, while being slightly more computationally intensive, because it can be based on theory rather than experimental approximations. Both multiple scattering and single elastic scattering were included because of the critical role that scattering processes play as the protons downscatter within the beryllium. Multiple scattering was implemented using the *G4hMultipleScattering* class.

3.3   GEANT Run Results & Analysis

In this section, the results of the GEANT simulation are presented and compared with expectations.

3.3.1   Expectations

The neutron energy spectrum is expected to look similar to that found in the following references. Amols & Dicello, [6], used 35 MeV protons incident on beryllium and lithium targets to produce the resultant spectra in the left plot in Figure 18. Curve A in this figure displays the neutron spectrum from the beryllium target. Howard *et al.* [18], presented neutron production spectra for protons at much lower incident energies (3-5 MeV), as displayed in the right plot in Figure 18. It would be expected that the GEANT simulation should fall somewhere between the 5 MeV and the 35 MeV experimental data.
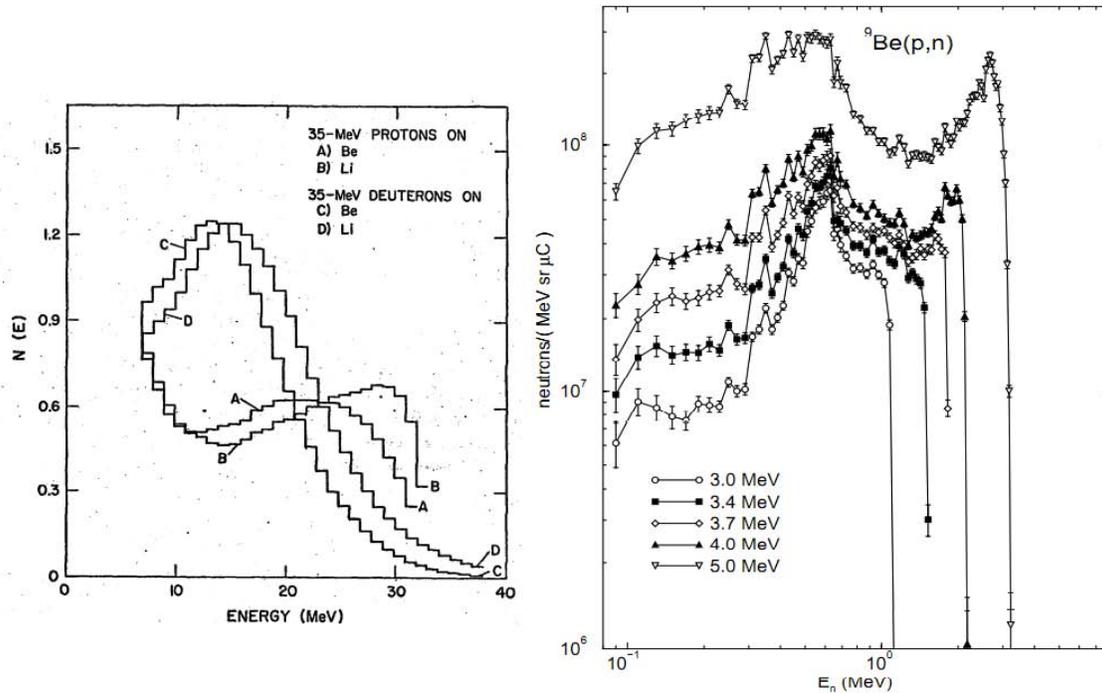
Figure 18. <u>Left:</u> Amols and Dicello[6] found the spectra of neutrons produced by stopping 35 MeV protons and deuterons in lithium and beryllium. The y-axis units in the left plot are $x10^9 \frac{neutrons}{MeV-sr-\mu C}$. <u>Right:</u> Howard *et al.* [18] produced a neutron spectra for a variety of low energy bombarding protons in beryllium.

It is also expected that the inelastic scattering neutron production reaction is biased in the forward-scattering direction [25]. This will be investigated further in Section 3.3.2.3.

3.3.2 Results and Comparison

The simple geometry simulation was conducted on a laptop computer as well as the IU supercomputing cluster, Quarry. The laptop computer was a Macbook Pro with a 2.26 GHz Intel Core 2 Duo processor and 2 GB of 1067 MHz DDR3 memory. The IU cluster is a collection of 140 IBM HS21 Blade servers, each containing two 2.0 GHz Intel Xeon 5335 quad-core processors, and 8 or 16 GB of memory. Users of the supercluster can use up to 336 cores (*i.e.* 1 job of 336 cores or 336 jobs of 1 core). Both

46

computers used version 4.9.3 of GEANT with patch 01 applied (*GEANT4.9.3-p01*).

3.3.2.1   Simulation Performance Statistics

A total of 52 runs were completed with $10^6 - 10^7$ primary particles simulated per run. The simulation used a quasi-randomized Monte Carlo seed such that the results of all runs are statistically unique. This amounted to a total of 1.91×10^8 protons simulated. The protons produced $1.81 x 10^5$ neutrons, therefore 0.95 neutrons are created per 1000 incident protons. This value is contrary to literature. Lone [29] fit an equation to experimental data of total neutron yield, Y_N, as a function of incident proton energies,E_p, as

$$Y_N(E_p) = 3.42 x 10^8 (E_p - 1.87)^{2.05} \, [\text{n}/\mu\text{C}]$$
$$Y_N(13 MeV) = 4.78 \times 10^{10} \frac{N}{\mu C}. \tag{23}$$

The neutron yield expected from 13 MeV protons is 4.78×10^{10} N/μC. If the elementary charge is $1.602 x 10^{-19}$C, then there are $6.2415 x 10^{12}$ protons per μC. Thus, according to Equation 23, one would expect 7.66 neutrons produced per 1000 protons, which is different from the yield found through simulation by a factor of 8.

3.3.2.2   Neutron "Birth Spectrum"

The simulation produced a neutron "birth spectrum," and it is displayed in Figure 19 and compared with the spectra found in literature. The birth spectrum does not compare well with the calculations [25] for 13 MeV protons. On average, the simulation is 700% lower than the values reported in [25]. Considering the factor of 8 difference in neutron yield between literature and the simulation results, it is to be expected that the magnitude of the neutron birth spectrum would be low. In addition, the shape of the spectrum is missing key components that are evident in

47

the calculations such as a ^{10}B* resonance induced neutron production peak at approximately 2.5 MeV as well as an increased number of neutrons at energies below 2 MeV. This could be an artifact of the smaller number of neutrons created per proton, *i.e.* the lower energy tail could be filled in with better counting statistics, or it could be indicative of problems in the physics simulated. Further study is necessary to determine the exact cause of these differences.
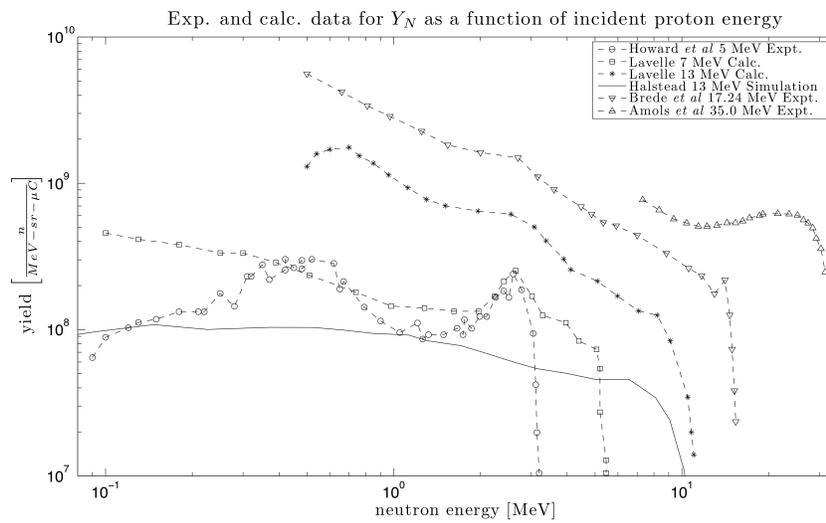
Figure 19. The results of the GEANT simple geometry simulation are compared with literature.

In Figure 20, the GEANT simulation is compared with the MCNP spectrum, as well as the calculations performed for 13 MeV protons incident on beryllium [25]. Again, the shape and magnitude of the simulation spectrum deviates significantly from the calculations and the MCNP simulation. Despite these differences, the neutron production spectrum produced by GEANT was used as an initial guess for the SAND-II unfolding code.

48
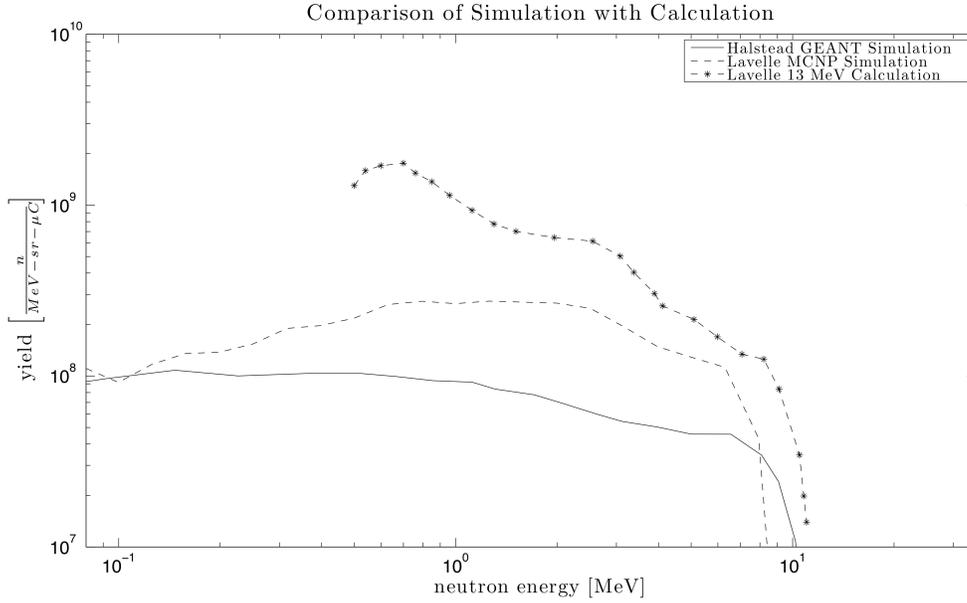
Figure 20. A comparison of the two simulation models with the calculations done in [25].

3.3.2.3 Neutron Initial Momentum Direction

To statistically analyze the initial momentum direction of neutrons created in beryllium, the coordinate axes must first be defined. Figure 21 shows the definition of θ and ϕ, where θ is the defined as the angle in the xy plane and ϕ is the angle in the yz plane. If a particle enters the frame of reference from the $+y$ direction and impacts a beryllium atom at the origin, θ is defined as the angle of the momentum vector of the produced neutron in the x-y plane. In this case, $0 \leq \theta \leq \pi$ is considered forward scattering, while all other angles are back scattering. The polar angle, ϕ, is the angle of inclination from the z-axis and can be described as how much the particle is deflected in scattering. It follows that $0 \leq \phi \leq \pi$, where $\phi = 0$ would imply scattering along the positive z-axis.

Figure 21 is the result of applying this ordinate definition to one of the simple

49
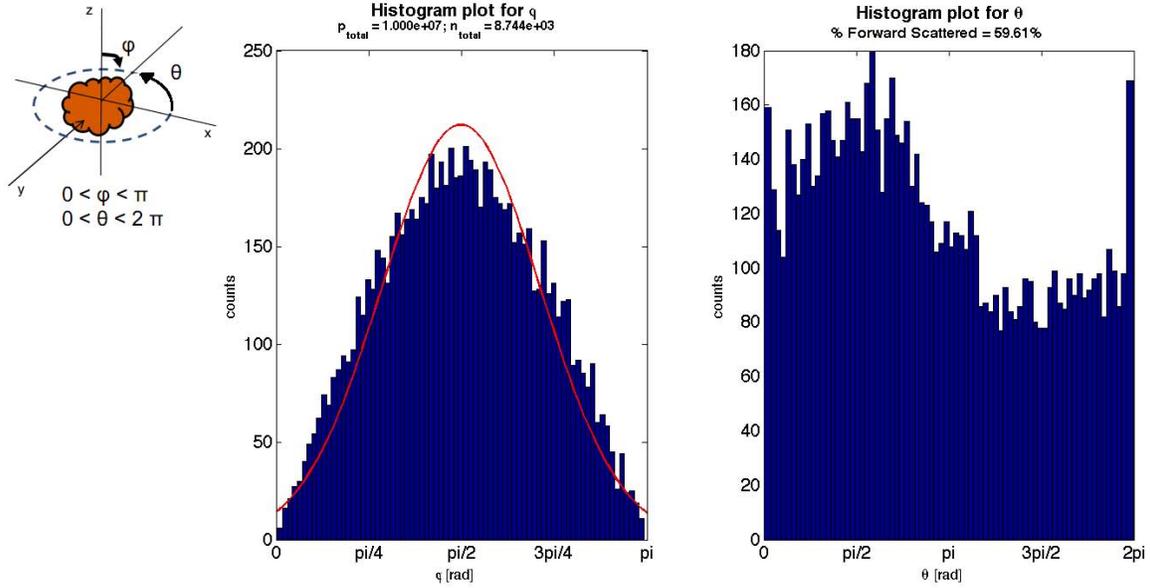
Figure 21. The polar, ϕ (left), and azimuthal, θ (right), angles of the neutrons born from inelastic scattering of protons in beryllium.

GEANT simulation run results for 10^7 protons simulated. It supports the conjecture that the inelastic scattering reaction produces forward biased neutrons, as 59.61% of the 8577 neutrons produced are scattered into the 0-π range. Additionally, the declination follows a roughly normal distribution with a peak near $\frac{\pi}{2}$, however it has been somewhat flattened.

The flattened shaped of the neutron birth angle distribution can be explained by considering the neutron birth locations. Figure 22 displays where neutrons are born within the beryllium sphere for one simulation of 10^7 protons, which produced 8744 neutrons. As displayed in the three plots to the right in the figure, neutrons are not "born" purely along the y-axis. This is due to proton scattering within the beryllium sphere. The scattering changes the protons' momentum vector, potentially adding an x-axis and/or a z-axis component. Even if the neutron is born into an angle on or near the $\frac{\pi}{2}$ declination angle, the addition of an x- or z-axis component to the momentum smears the distribution to the flattened shape displayed in Figure 21.

50
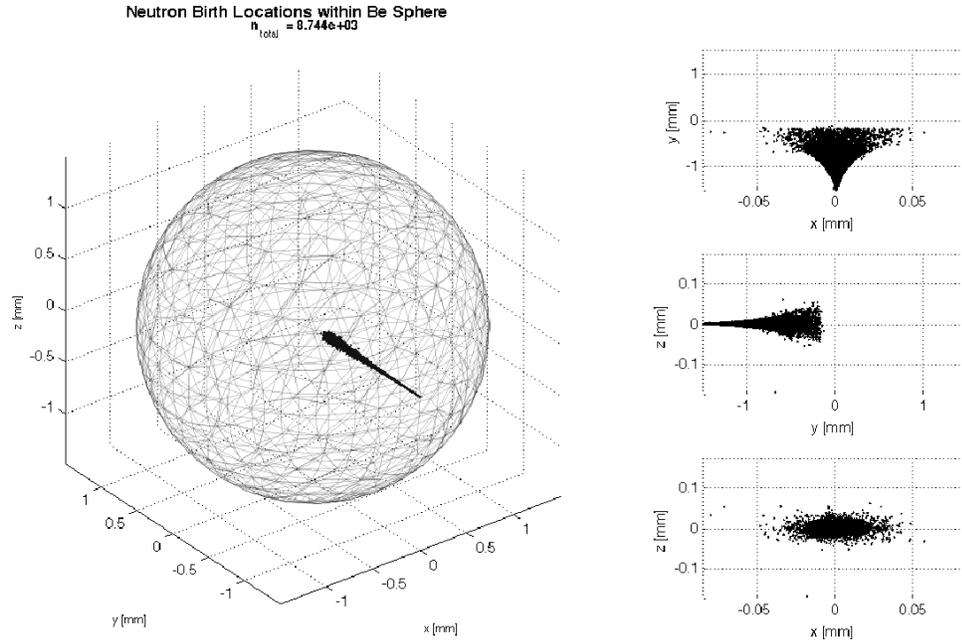
Figure 22. <u>Left:</u> **The birth locations of neutrons in 0.15 cm radius beryllium sphere due to 13 MeV protons; protons are incident on sphere in the positive y-direction.** <u>Right:</u> XY, YZ, **and** XZ **plane cuts showing the birth location of neutrons in the beryllium sphere. Units in all plots are mm.**

51

IV. Experiment

Neutron activation analysis experiments were accomplished to determine the activity at saturation of multiple elements induced by the NREP neutron production source. This data was then used in the SAND-II code for spectral unfolding to produce an estimate of the observed neutron energy spectrum. In the following section, the experimental set-up will be described, data presented, and results analyzed.

4.1 Experimental Equipment

The experiment set-up included two locations: the irradiation site and the activity measurement site. The irradiation site included the proton LINAC, NREP TMR, and the stringer that positioned the foils and wires in the neutron flux. The proton LINAC, discussed in Section 1.2.1, was developed at Indiana University, and a picture of it is displayed in Figure 23.
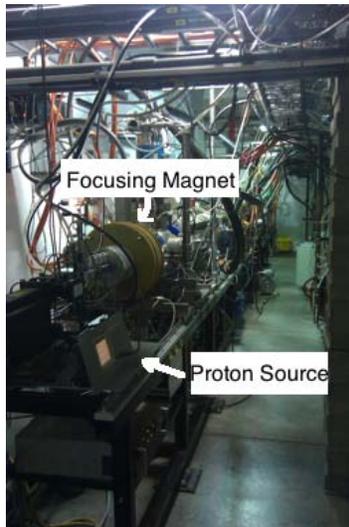
Figure 23. The LINAC that accelerated protons from rest to 13 MeV using an RFQ and two DTL sections started at the proton source.

The NREP TMR is a cylinder made up of three primary components: the target assembly, primary decoupler shielding, and vault shielding. The target assembly is at the end of the beam line and constitutes the end cap with the target positioned inside the vacuum beam line. The target assembly is made from an aluminum case that houses the beryllium target and the cooling water channel behind it. The primary decoupling shielding material is a hollow cylinder that surrounds the end of the beam line and target assembly, and it is made from 30% (by weight) borated polyethylene blocks that surround a lead enclosure. This layer absorbs a significant portion of neutrons and gammas, respectively, in order that the vault shielding sees much less radiation. This vault shielding, made from a layer of borated epoxy lead bricks and 2% (by mass) borated polyethylene bricks, is in place to limit the radiation exposure of anything in the TMR vault during beam operation. In this way, various devices can be kept in the vault with only minimal additional radiation shielding. A picture of the blocks of borated material in the outer shell of the NREP TMR is displayed in Figure 24.

A picture of the stringer used to situate the irradiation samples approximately 2 cm downstream of the beryllium target is shown in Figure 25. This stringer allowed the experimenter to reproducibly position the samples before sliding it into place inside the TMR.

After irradiation, the samples were relocated to the activity measurement site. This station consisted of a High-Purity Germanium (HPGe) detector connected to a personal computer via a Canberra LynX analysis box. The computer used the Canberra APEX software suite. Table 4 presents the relevant equipment data.

A HPGe detector is a common piece of equipment used in gamma counting experiments. At the IU CEEM, the detector is a standard coaxial electrode configuration, a

Figure 24. The outer shell of the NREP TMR is made from blocks of borated materials used to absorb neutrons and limit the radiation exposure to equipment located outside the TMR cylinder.
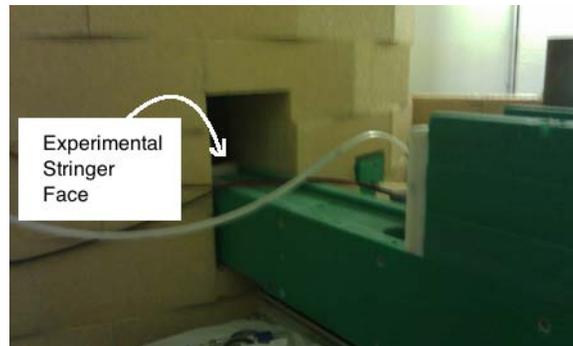
Figure 25. The experimental foils and wires were set on the front face of a stringer, displayed in the right of the picture above.

Table 4. Data collection equipment information.

Item	Producer	Model	Serial #
HPGe Detector	Canberra	GC7020	1300000026
HPGe Detector Shield	Canberra	747	130000026
Digital Signal Analyzer	Canberra	LynX	130000224
Software Suite	Canberra	APEX	v1.2 (1 Nov 07)

picture of which is displayed in Figure 26. In this configuration, n-type contact material at the edges of the germanium and p-type contact material at the core (typically diffused lithium and implanted boron, respectively) act such that applied reverse bias totally depletes the intrinsic germanium material in between. Charge carriers created by incident gammas are swept to the electrodes and converted to a voltage pulse by a built-in preamplifier.
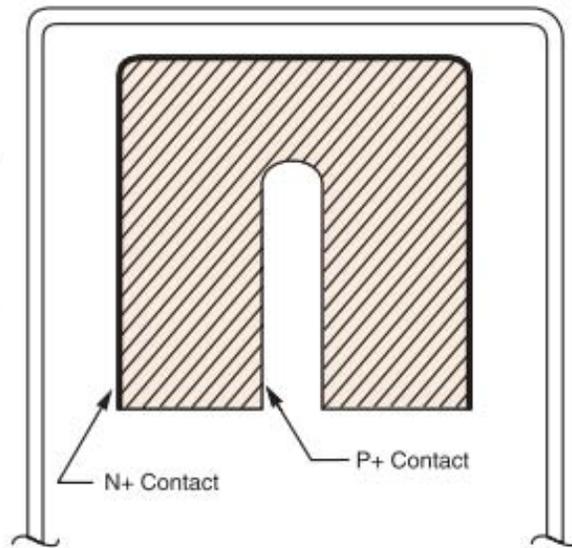
Figure 26. The schematic for a Standard Electrode Coaxial Germanium Detector displays an n-type contact and p-type contact sandwiching high-purity germanium (crosshatched area) and surrounded by a cylindrical metal shell.

All electronics required for a gamma detector (such as signal conditioning, analog-to-digital converter, spectral memory, and high-voltage power supply) were contained within the LynX multi-channel signal analyzer. The analyzer was connected to a computer running the Canberra APEX software suite, which in turn used the proprietary Genie™2000 gamma analysis software.

4.2 Design of Experiment

4.2.1 Calibration

Before beginning experiments at the IU CEEM, the gamma detector was calibrated for background, energy, and efficiency corrections. Every two to four weeks after that, the equipment was recalibrated to ensure continuity of the data sets. To calibrate for background, all sources were removed from the detector and a one-hour measurement performed. The resultant spectrum was saved and automatically removed from all subsequent data taken by the APEX software suite.

Energy calibration was accomplished to associate multichannel-analyzer bin numbers to energy values. This was done using a standard source. The IU CEEM uses a National Institute of Standards and Technology (NIST) traceable tri-nuclide source containing two isotopes of europium and one isotope of cesium. After taking an hour-long measurement, gamma peaks of known energy can be associated with particular energy bins and an energy calibration curve developed.

Finally, the detector efficiency was calibrated using a built-in geometry composition program, as well as a pre-imported certificate file for the tri-nuclide source. The geometry tool calculated solid angle and the certificate file provided the gamma ray intensities, both of which factored into determining the efficiency. These calibration steps were accomplished in order to minimize counting error in the system and to increase the likelihood of repeatability of measurements, if needed.

4.2.2 Experiments

The purpose of the experiments was to determine induced radioactivity in various materials. The first set of experiments were run to support a decision regarding the number and location of foils/wires that could be included on a single irradiation sample. To this end, gold foils were situated at regular intervals across the face of

56

cardboard backing, which was adhered to the stringer face using tape. Foils were numbered 1 - 16 for tracking purposes. A schematic is shown in Figure 27.
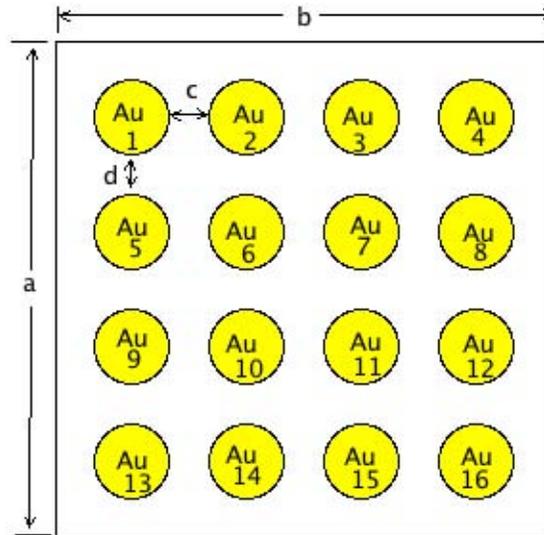
Figure 27. The schematic of an irradiation sample for gold foil measurements; dimensions: a = 12.7 cm, b = 14.6 cm, c = 2.2 cm, d = 2.0 cm.

The height and width of the irradiation samples were 12.7 and 14.6 cm, respectively. The distance between gold foils was 2.0 cm, vertically, and 2.2 cm, horizontally. The gold foils were circles of approximately 1 cm in diameter and 1.27×10^{-3} cm thick. Before placement of the sample, the mass of each foil was measured using a Sartorius CP224S Digital Scale. The mass data can be found in Appendix A.

Two samples were irradiated, one using bare gold foils at each placement location and the other with cadmium coverings for each foil. The cadmium thickness ranged from 0.414 to 0.610 cm, measured using a micrometer. The beam operating parameters for each measurement are summarized in Table 5. The results of this experiment can be found in Section 4.4.

Table 5. NREP beam parameters for gold foil measurements.

Parameter	Value
E_p	13 MeV
I_{beam}	20 mA
f_{beam}	20 Hz
Pulse Width	$400\mu s$
Klystron Power	~ 2 kW

4.2.2.1   Material Location Selection

Once this experiment was finished, irradiation locations were selected and the main experiment was accomplished. The main location of interest was selected based on the location of the highest total induced activity. Four other locations were selected to measure the spatial variation across the stringer face. A schematic of this is displayed in Figure 28. One foil/wire was placed in the center (7.3 cm from the left edge and 6.8 cm from the top edge), as this was where the highest total activity was induced, and one foil/wire was placed 3.81 cm from the center in each cardinal direction for spatial variation measurements. To do bare foil irradiations, a single sheaf of paper ($t \approx 0.1$mm) secured by tape held the sample material in place. For cadmium covered irradiations, the cadmium covers with sample material inside were adhered to cardboard using tape.

If the material being irradiated was a foil, efforts were made to place it's center point at the center point of the location chosen. However, shifting was expected, and an error of $\pm 1 - 2$ mm is possible. If the material was a wire, shifting was expected to cause the material to orient itself parallel to the floor. Thus, the wire could also be 1-2 mm south of the center point for the particular location.

The main experiment was designed such that the maximum number of material irradiations could be accomplished. Each cardboard sample with five materials was irradiated in the beam for approximately two hours, at which time the sample was

58
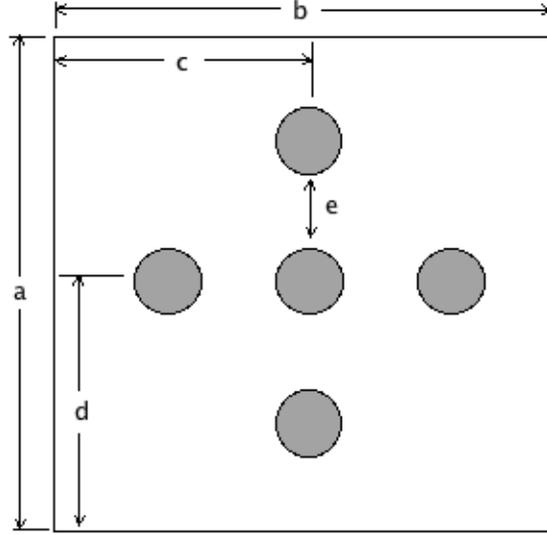
Figure 28. The schematic for an irradiation sample of foil/wire measurements; dimensions: a = 12.7cm, b = 14.6 cm, c = 7.3 cm, d = 6.8 cm, e = 3.8 cm.

relocated to the gamma measurement system location. For a particular sample, each foil/wire was removed from the cardboard backing and individually placed in the HPGe detector. The total gamma spectrum was sampled for 20 minutes. In some cases, the counting time was increased to 2-6 hours to obtain better counting statistics. Due to the intensity of radioactivity induced in some materials, the foils/wires were suspended at various heights above the germanium crystal to minimize dead time in the detector. Detector efficiency calibrations were accomplished for each suspension height: 8 cm, 15 cm, and 23 cm.

The counting data was converted to activity (corrected to saturation) via the method described in Section 2.3.3. To reiterate Equation 16, the activity at saturation is

$$A_\infty = \frac{\lambda(C - B)}{\epsilon \left(1 - e^{-\lambda t_0}\right) e^{-\lambda t_0} \left(e^{-\lambda t_1} - e^{-\lambda t_2}\right)}, \tag{24}$$

where C is the number of counts measured in the counting interval, B is the background counts, ϵ is the detector efficiency, t_0 is the irradiation time, $t_1 - t_0$ is the wait

59

time between irradiation and counting, and $t_2 - t_1$ is the counting time. Since B and ϵ are accounted for by the APEX software suite and time increments are known, the number of counts can be inserted directly into the equation to solve for A_∞. The SAND-II code requires activity in $\frac{disintigrations\ per\ second(dps)}{atom}$, therefore each activity was divided by N_i, the number density of atoms originally present in the *ith* material. This is calculated using $N_i = \frac{\rho_i N_a}{M_i}$ where ρ_i is the bulk material density, N_a is Avagadro's number, and M_i is the atomic weight. The data for each sample irradiation was collected in a spreadsheet that served to accomplish calculation steps as well as to act as a data repository. These data points were processed using the SAND-II computer code for unfolding of spectra.

4.2.2.2 Irradiation Foil Materials Selected

In deciding the materials to use in this irradiation study, it was determined that the best course of action was to select a number of materials that were both *full-spectrum* and *threshold* detectors. Selecting a number of threshold detectors, which require neutrons with at least a minimum amount of energy before the reaction can occur, aids the SAND-II code to unfold the spectrum, as it provides extra data on the number of neutrons above a certain energy barrier. Examples of threshold detector reactions include $^{27}Al(n,p)^{27}Mg$ and $^{58}Ni(n,p)^{58}Co$ with neutron threshold energies of 1.9 MeV and 1 MeV, respectively. The materials selected for use in these experiments are displayed in Table 6. A number of different materials were used in an effort to cover as much of the spectrum using materials readily available.

In Table 6, the reaction column implies that not all reactions were (n, γ) interactions, while a HPGe detector was used to measure activity. This is due to the type of neutron activation analysis accomplished. Neutron activation can be broken into a number of sub-categories. Prompt Gamma Neutron Activation Analysis (PGNAA)

Table 6. Materials selected for use in the main experimental analysis (TE is *threshold energy*).

Activation Reaction[1]	Radioactive Product	Half-life	Threshold Energy (MeV)[2]	Geometry
^{27}Al(n,p)	^{27}Mg	9.46 min.	1.89632	Wire
^{27}Al(n,α)	^{24}Na	15 hr.	3.24900	Wire
^{59}Co(n,α)	^{56}Mn	2.5785 hr.	N/A	Wire
^{59}Co(n,γ)	^{60}Co	5.2714 yr.	N/A	Wire
^{63}Cu(n,γ)	^{64}Cu	12.700 hr.	N/A	Wire
^{115}In(n,n$'$)	^{115}In	4.486 hr.	N/A	Foil
^{115}In(n,γ)	^{116}In	54.29 min.	N/A	Foil
^{56}Fe(n,p)	^{56}Mn	2.5785 hr.	2.96566	Foil
^{54}Fe(n,p)	^{54}Mn	312.3 d.	N/A	Foil
^{58}Fe(n,γ)	^{59}Fe	44.503 d.	N/A	Foil
^{58}Ni(n,p)	^{58}Co	70.86 d.	1.00000	Wire
^{109}Ag(n,γ)	^{110m}Ag	249.79 d.	N/A	Foil
^{197}Au(n,γ)	^{198}Au	2.69517 d.	N/A	Foil

Note:
 [1]Each reaction includes a bare and cadmium covered scenario.
 [2]Data collected using Qtool [34]

measures the gammas emitted during neutron irradiation, while Delay Gamma Neutron Activation Analysis (DGNAA) measures the gammas emitted by the metastable isotopes created by neutron irradiaiton. It is DGNAA, not PGNAA, that was done in this work. Thus, a reaction such as neutron capture by ^{59}Co resulting in ^{56}Mn and an alpha emission was used because ^{56}Mn emits an 846.7 keV gamma almost 100% of the time with a half life of 2.58 hours.

4.3 Precision Timing Using a Fission Chamber Detector

It was discovered, during preliminary experiments, that the electronic log file that tracks beam operation infrequently reported operational parameters such as beam current and ion source coolant temperature. Because of spurious high voltage causing the beam line to turn off, long-term irradiations were not possible. In essence, unless the experimenter stood at the control console and watched for any inadvertent beam

trips, it was possible to lose track of when the beam turned *off*. This was because the short and long term automatic electronic logging only recorded in intervals of one and ten minutes, respectively. If, for example, an irradiation experiment was started late in the evening with the expectation of running overnight and the beam tripped in the middle of the night with no one watching, it was not possible to determine, with sufficient precision, when the beam was on and when it was off.

To this end, a simple system of tracking the beam operational status was devised. At an alternate beam port on the NREP TMR, a small fission chamber detector was positioned. The fission chamber detector, as described in Section 2.2.5, produces counts when thermal neutrons interact in the detector volume and cause a fission event. Using a simple electronic set-up and a LabView program to control the system and record the data, beam timing could be measured to within approximately one second (± 0.1s).
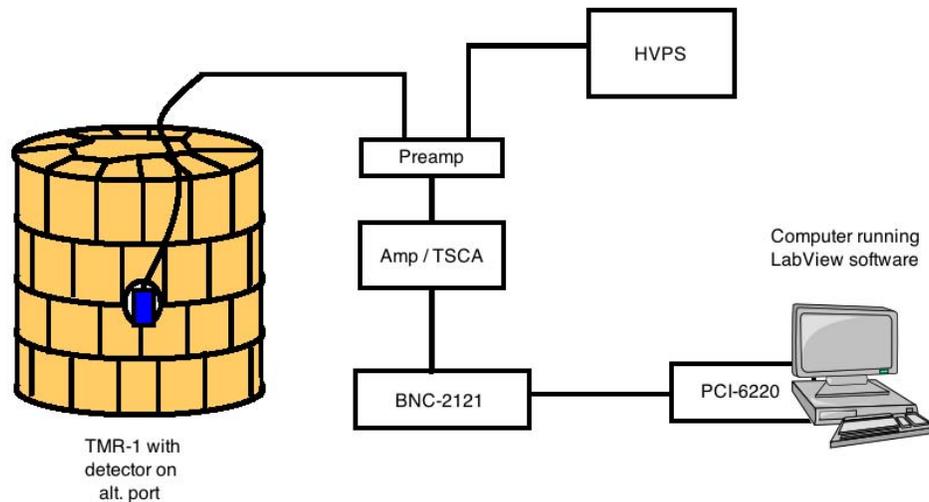
Figure 29. A schematic drawing of the fission chamber timing system shows its component electronics.

A schematic of the electronics for the fission chamber measurement system is shown in Figure 29. The timing system used an ORTEC Model 142c preamplifier to

condition the signal. The signal was fed into an ORTEC Model 590a Amplifier and Timing Single-Channel Analyzer (TSCA) for amplification and further conditioning. The fine gain and coarse gain on the Amplifier were set to 0.5 and 20, respectively; thus, the total gain in the system was 10. The TSCA was set to window mode with its lower level discriminator set to ignore system noise (+1.2 V) and it's upper level discriminator set to the highest setting. The conditioned signal then travelled to the National Instruments BNC-2121 Connector Block. The connector block acted as a "break-out box" for the signal, replacing the BNC signal-carrying cable with braided copper wire, where it was passed into a National Instruments PCI-6220 M Series data acquisition board connected to a PC running LabView.
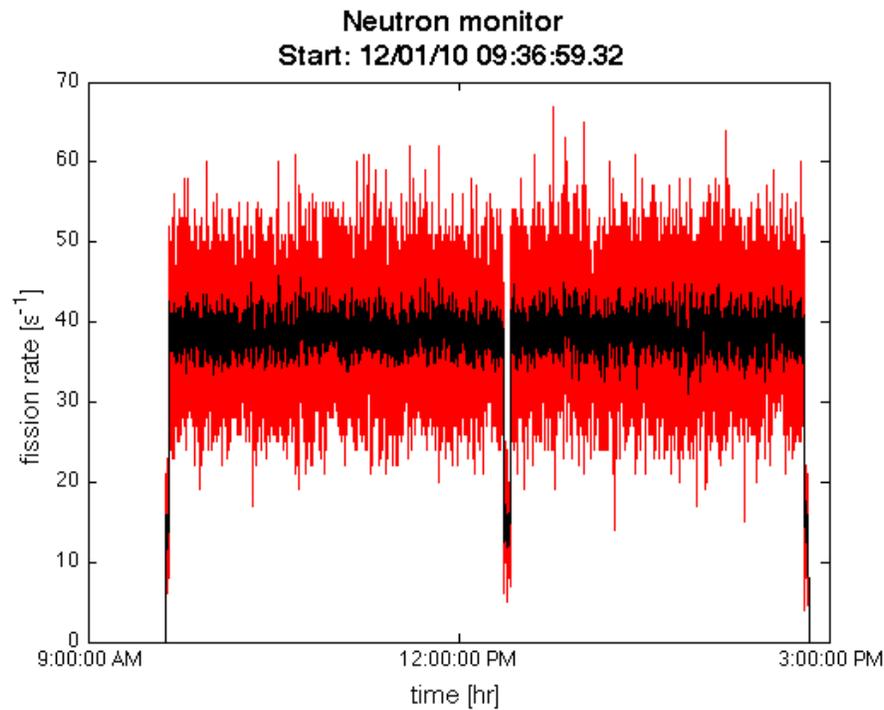
Figure 30. The plot resulting from post-processing of the number of fission counts per time bin (in this case, one second); the red points are instantaneous fission rates, while the black points are rates averaged over ±4 seconds to suppress signal noise.

63

A program was written to collect and record the data. Finally, the data file was post-processed by a script that analyzed it for *on* and *off* signals. An example of the figures produced by the post-processor is displayed in Figure 30. Due to significant noise in the system, the instantaneous fission rate was time-averaged over 8 surrounding points. In this figure, the irradiation start time is displayed as 09:36:59.32. It then trips at approximately 12:30pm and is reset about 10 minutes later. The beam is shut down around 3:00pm for transition to the next sample. The post-processing script also produced a list of on and off times in addition to the plot, so approximation was not necessary. The plot was used to verify the on/off time list to minimize timing errors.

4.4   Gold foil Spatial Comparison

A set of two irradiations utilizing gold foils (one bare and one with cadmium covers) was accomplished. The activity was calculated using the methods described in Section 2.3.3. Since gold is a full-spectrum detector, the total flux cannot be directly determined from these measurements alone. The total activity at saturation depends on neutrons of all energies, therefore energy dependence cannot be overlooked. However, a measure of the activity at various points on the stringer face can provide a good estimate of where the highest total flux is observed.

Gold is a common material used for foil irradiations due to its appreciable capture probability at all relevant energies. Also, the gold capture reaction, $^{197}\text{Au}(n,\gamma)^{198}\text{Au}$, has no threshold energy, as is discussed in Section 2.3.1. Therefore, it is possible for neutrons of any energy to induce capture and subsequent gamma emission. A plot of the neutron capture cross-section for ^{197}Au is displayed in the plot on the right in Figure 31.
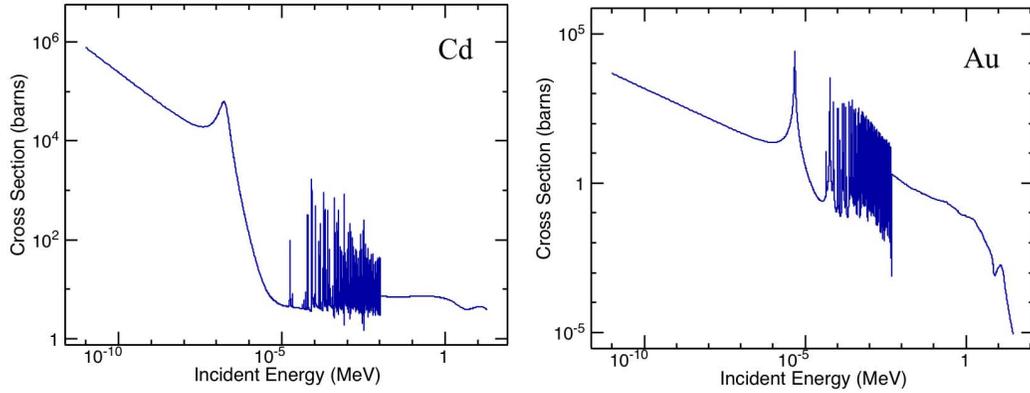
Figure 31. <u>Left:</u> **The total cross section for** [113]**Cd for thermal through fast incident neutrons shows the cadmium cutoff, around 0.5 eV [1].** <u>Right:</u> **The cross section for** [197]**Au for the (n,γ) reaction [1].**

4.4.1   Bare Gold Foil Measurement

The first irradiation used the sample schematic displayed in Figure 27. The foils were only irradiated for 16 minutes due to a high-voltage trip, which induced beam shut down. This issue will be discussed further in Section 5.1.2. Activity at saturation was calculated and the activity is tabulated in Table 7. Note that the highest activity at saturation is located roughly in the center of the stringer face (locations 6-7 and 10-11). For this reason, the center location was selected as the target location of greatest interest for this research.

Table 7. **Total activity, corrected to saturation, induced in gold foils by 16 minutes of beam time at 16 locations defined in Figure 27.**

Loc.	Total Activity $\times 10^{-13}$ [dps/atom]	Loc.	Total Activity $\times 10^{-13}$ [dps/atom]
1	2.650	9	3.201
2	3.058	10	4.057
3	3.557	11	4.202
4	2.515	12	3.146
5	3.016	13	2.937
6	3.731	14	3.509
7	4.101	15	3.541
8	3.057	16	0.275

65

4.4.2   Cadmium-Covered Gold Foil Measurement

As discussed in Section 2.3.2, the activity due to thermal neutrons, A_{th}, can be described by Equation 10 as

$$A_{th} = A_m - F A_{Cd}, \tag{25}$$

where A_m is the measured activity of the bare foil, F is the resonance escape factor (1.056 for boron with thickness of 20 mils), and A_{Cd} is the measured activity of the cadmium-covered foils. The thermal flux can then be calculated by Equation 12.

Table 8.   Stringer thermal flux calculations at locations 1–4 based on experimental measurement.

Loc.	A due to Φ_{total} [dps/atom]	A with Cd-Cover [dps/atom]	A due to $\Phi_{thermal}$ [dps/atom]	% of Φ_{total}
1	2.6496E-013	2.4189E-013	9.5225E-015	3.594%
2	3.0582E-013	1.8391E-013	1.1161E-013	36.496%
3	3.5574E-013	2.2126E-013	1.2209E-013	34.320%
4	2.5152E-013	1.4148E-013	1.0212E-013	40.601%

Due to data corruption encountered when using the gamma collection equipment, the only activity values recorded for the cadmium covered gold foil measurements are for positions 1-4, as displayed in Figure 27. The thermal flux was calculated using Equation 10 for these four points and is displayed in Table 8. Flux is depressed approximately 37% when comparing thermal to total flux for three of the four points; the foil located in the top left (position 1) only displays a 4% activity depression. This could be due to the thermal flux being lower at this point or experimental error.

4.5 Irradiation Results

The main thrust of this research was to collect enough foil activation data to be input into the SAND-II computer code for the five selected locations displayed in Figure 28. The user's manual did not specify a particular number as being minimum or optimal, however it notes that ten or twenty foil activity data points are typically used [30]. As described in Table 6 within Section 4.2, seven materials were used, which covered thirteen reactions. Therefore, there was the possibility of including up to 26 total reactions in the SAND-II input deck, when cadmium covers were considered.

Table 9. Excerpt from spreadsheet for data analysis.

...	Counts	$\pm(\%)$	A_{CS} dps	A_{SAND} (dps / atom)	A_{low}	A_{high}
...	1.34E+06	0.09%	1.9128E+05	1.59046E-16	1.58903E-16	1.59189E-16
...	7.87E+05	0.11%	126871.09	1.05057E-16	1.04942E-16	1.05173E-16

Samples were irradiated for approximately two hours, sometimes with intervals of beam down-time included due to tripping of the high voltage power supply. For each irradiation, a spreadsheet was maintained as a repository of material mass data, experiment time interval information, gamma count data, and induced foil/wire activity calculations. Table 9 displays an excerpt from the data analysis spreadsheet (see Appendix B for a full example of this spreadsheet). The ellipses in Table 9 are denoting that there are data values in cells to the left. Note that the saturated activity, A_{CS}, and the activity per atom, A_{SAND}, are calculated for each foil/wire. Also calculated is the lower and upper bounds for A_{SAND} based on the gamma count uncertainty provided by the APEX software suite. This data was fit and uncertainty was calculated using the Non-linear Least Squares (NLLS) method. In this method, the data are approximated by a quadratic model with some initial parameters. The model is refined by successive iterations until a solution is reached. Error is collected in the *residuals*.

67

```
Datasource   : C:\CANBERRA\APEX\ROOT\INDIANA_UNIVERSITY_CYCLOTRON\DATA\0000000567.C
Sample ID    : Halstead20101206              Iterations   : 0
Sample Date  : 12/06/10  5:42:36 PM          Chi-square   : 0.00
Fit Engine   : Sum / Non-Linear LSQ Fit      Region Start : 840.703 keV
Bkgnd Type   : Step                          Region End   : 851.863 keV

Nbr     Energy  Centroid       Area   %Error     FWHM   Ratio
 1     846.358  2350.71  637136.94     0.13    1.410    1.01
```
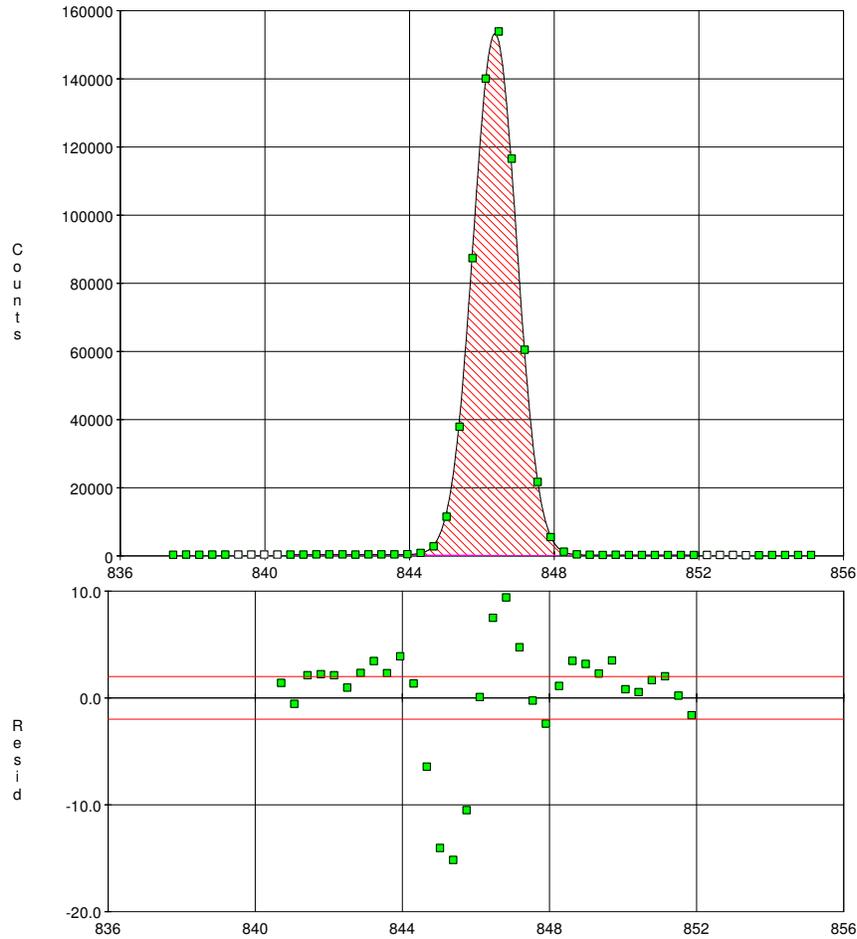
Figure 32. The APEX software suite calculated a peak fit for the gamma counts in order to determine the counts due to each particular gamma ray energy, and this fit is representative of the results obtained.

68

Figure 32 shows an example of the peak fitting results. In the figure, there are two aspects of note. First, the data in the header presents a variety of identification information. For example, the type of fit engine used is named as NLLS in this case. The peak energy of 846.358 keV, the number of counts at the centroid (2350.71, a fraction because it interpolates between two channels), the number of counts under the peak area using the fit ($6.37x10^5$), the error due to counting statistics (0.13%), the Full-Width Half-Max (FWHM) of 1.41 keV, and the Gaussian ratio (1.01) are all displayed in the header. The FWHM provides a measure of the energy resolution of the system. The Gaussian ratio is a measure of the "goodness-of-fit" to the curve produced by the NLLS fit, in which a value of 1 is desired. As the Gaussian ratio approaches unity, the fit becomes better.

The second aspect of Figure 32 to note are the plots. The middle plot displays the gamma counts measured by the detector as well as the fit line found by the NLLS routine. Below that, a plot of the residuals shows how the fit deviates from the actual measured gamma count rates for each energy bin, in terms of sigma deviation. The fit is better if the residuals are smaller.

After fitting each of the peaks for a measured gamma spectrum, the number of counts found under the fit curve are calculated and used in Equation 16 to solve for A_∞. The data for each foil/wire location was then collected in a spreadsheet (an example of can be found in Appendix B) and input into the SAND-II code for analysis and unfolding. The raw activity measurement data can be found tabulated in Appendix C.

4.6 SAND-II Analysis

The SAND-II computer code was used to deconvolve the neutron energy spectrum observed at the NREP TMR target area. After measurements were made and the

69

data analyzed to determine the activity corrected to saturation, an input deck was created. An example of a SAND-II input deck used in this work can be found in Appendix D.
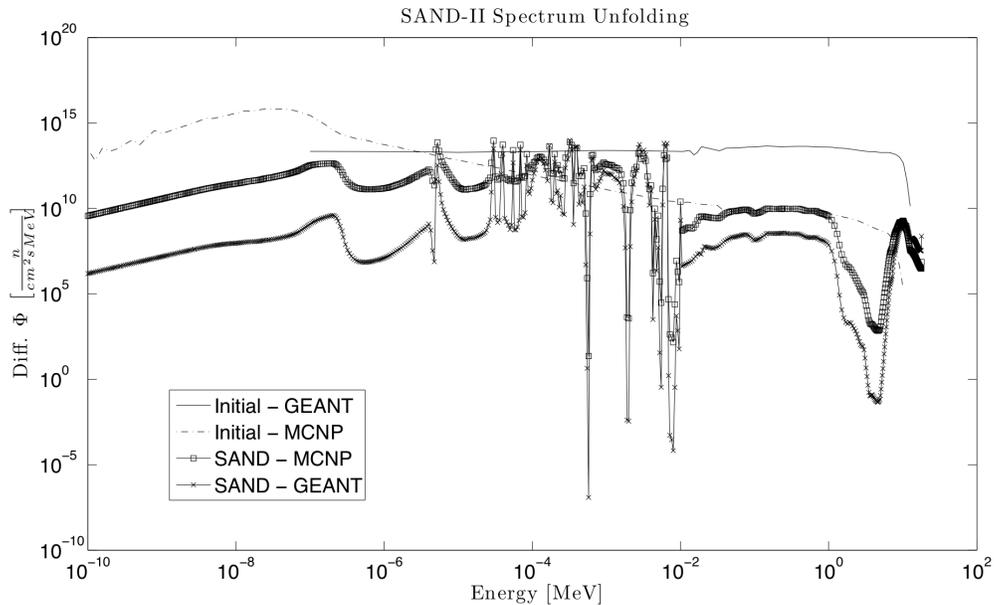
Figure 33. The differential neutron flux spectra produced by SAND-II using two different input spectra (MCNP and GEANT) are compared to the initial input spectra.

The results of analysis of the input deck are displayed in Figure 33, which shows a plot of the differential flux as a function of energy. A plot of the input guess spectra, the solid line (GEANT) and dashed line (MCNP), is displayed along with the calculated spectra to show how the unfolding code perturbed the spectrum to produce the results. The large resonance peaks in the epithermal region imply instability in the code solution, thus the resultant spectrum as provided by SAND-II is unreliable and should be studied further to determine how to resolve any issues.

70

V. Discussion

5.1 Conclusions

5.1.1 Remarks Regarding Simulation

A simple geometry simulation of the NREP beam line has been built in GEANT and the simulated neutron energy spectrum compared to literature, with the result being inconclusive. The shape of the spectra are similar; for example, the maximum neutron energy is correctly calculated to be at the expected value of 11 MeV based on the 2.05743 MeV [34] Q-value of the *(p,n)* reaction. However, comparison with literature ([25], [18], [6]) elicits questions.

First, spectra produced by both calculation and experiment show a resonance for $^{10}B^*$ at 2.56 MeV, which should create a noticeable peak in neutron production at this energy. This is not evident in the energy spectrum produced by the GEANT simulation. With no experimental data at these proton energies, it is difficult to determine whether the peak in the calculations [25] at 2.56 MeV is an artifact or if there is something missing in the GEANT physics, due to omission in the selected physics processes or intrinsically in the physics models incorporated in GEANT. Also, as the incident proton energy increases and more energy is available to the quasi-compound nucleus, neutrons of higher energy can be emitted as the excited nucleus decays to the ground state. Therefore, an increase in emitted neutron intensity in the epithermal and thermal regions is expected, but it is not evident in the GEANT simulation where the epithermal transition is characterized by a levelling of the spectrum. Again, without experimental information, it is difficult to argue the validity of the simulation or the calculations. For reference, both the simulation and literature results are displayed in Figure 19 in Section 3.3.2.2. Because of these discrepancies, it is recommended that the simulation be run at proton beam energies for which experimental

data is available, such as Howard *et al.* [18] at $E_p = 5MeV$ and Amols *et al.* [6] at $E_p = 35MeV$ to validate the model.

Despite these discrepancies, the model has proven that the reaction is biased towards forward-scattering, with 59.61% of the neutrons produced in the forward direction. Additionally, the reaction shows a tendency to small angles of deflection in ϕ. The distribution approaches normal, but it is somewhat flattened by a smearing effect caused by proton scattering within the beryllium imparting momentum in the x- and z-directions to the created neutrons.

When attempting to increase the fidelity of the model, mistakes in defining the new geometry caused the simulation to behave non-physically. Protons generated as primaries in the beam line impacted the NREP TMR shell at various shielding levels. This implies that the beam line vacuum does not penetrate the shells, but ends at the outer shell where the protons are stopped without reaching the beryllium target. Continued work is ongoing to fix the problem.

The MCNP model provided an input guess spectrum to be applied in the SAND-II calculations. However, as this spectrum is based on a different TMR (LENS instead of NREP) with a methane moderator between the target and sample irradiation location, it is expected that this spectrum is also incorrect. In addition, the spectrum is based on an "assumed" neutron production spectrum, which utilized theory to calculate the source neutron yield and angular dependence.

5.1.2 Experimental Issues

A major drawback that greatly hampered the ability to perform experiments consistently was erratic beam operation. Personnel at IU stated that, in the past, the beam could be run for weeks at a time without stopping. However, as new components have been added, the system is no longer as stable as it once was. Occasional

high-voltage transients now cause the beam line power supply to be cut, in turn effecting a *trip*. A picture of the inside of the capacitor bank storage facility is shown in Figure 34, which shows the large mechanical fuses that seem to be the source of the problem. To address the problem, the IU CEEM has ordered custom equipment that will arrive some time in 2011.
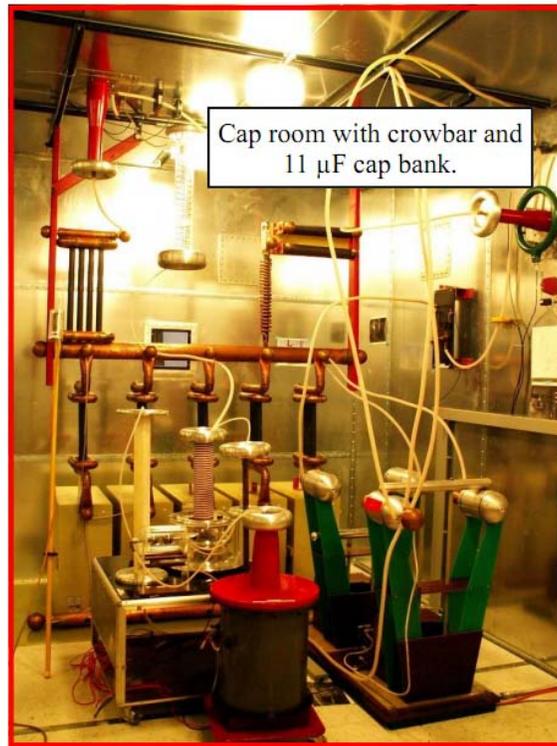
Figure 34. Inside the capacitor bank storage closet a series of mechanical, crowbar fuses keep the system from being damaged by voltage spikes; note the crowbar fuses in the lower right corner of the picture.

The analysis accomplished by the SAND-II unfolding code produced inconclusive results, and a discussion of these error modes is warranted if future work is to continue characterizing this facility. First, the measurement of induced radioactivity due to neutron bombardment relies heavily on an accurate measurement of timing. The amount of time under irradiation, the delay between irradiation and counting, and

the counting time. These must be known to properly account for all processes in the system. When the fuse tripped, it was difficult in some of the earlier measurements to accurately determine the amount of time under irradiation. This was corrected in later measurements through the use of a fission chamber detector to monitor and record the presence of beam on target.

Also related to timing is the proper accounting of induced activity due to a pulsed source, as opposed to that of a continuous source such as a nuclear reactor. The IU CEEM neutron source is a pulsed accelerator that only provides the full flux of neutrons for a ~1% duty time. During the remaining 99% of the time, other interactions are occurring; most notable of these is radioactive decay. In an attempt to mitigate this error, an assumption was made that during any particular irradiation, the actual irradiation time is the total time that the beam is on. To provide insight into the effect of this assumption, a simulation was built by which a series of linear equations was solved. When the beam was on, the equation was

$$A^i_{on}(t) = R \left(1 - e^{-\lambda t_{on}} \right), \tag{26}$$

and when the beam was off, the equation was

$$A^i_{off}(t) = A^{i-1} \left(e^{-\lambda t_{off}} \right). \tag{27}$$

Figure 35 shows a plot of the resultant activity curve. Due to the method of simulation chosen, increasing amounts of simulated time caused the computation time to increase exponentially. Therefore, only 2.5 seconds was simulated. At first glance, the two curves closely meet at the terminus, as is shown in Figure 35. This implied that the assumption was valid. However, upon further examination, there are small differences due to radioactive decay between pulses.

74
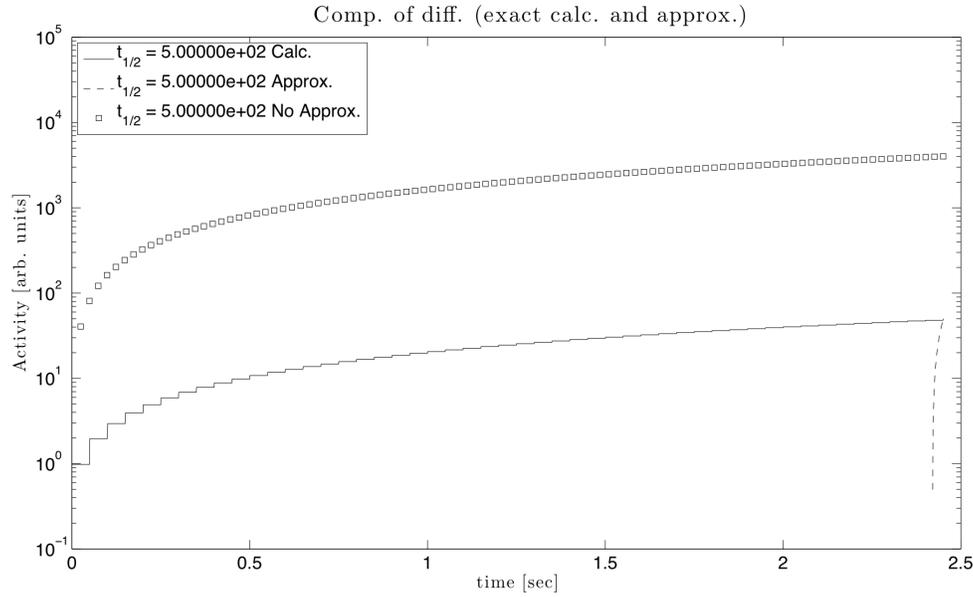
Figure 35. A comparison between three scenarios for activity induced due to a pulsed neutron source: exact calculation, approximation that irradiation time is duty cycle of beam, and no approximation applied (*i.e.* irradiation time is time beam is on).

While these differences have been noted, they were considered negligible and were assumed not to affect the results because of the relatively short irradiation periods. To make this assumption, the following reasoning was used. It can be seen that short half-lives induce the largest differences due to increased decay during beam *off* periods, and this is plotted in Figure 35. The shortest half-life for a daughter product produced by the neutron activation experiments was ^{27}Mg, whose half life is 9.4 minutes or 564 seconds. Also, the longest irradiation time was approximately 3 hours, or 10800 seconds, which corresponds to 108 seconds of actual irradiation (beam duty time). The half life and irradiation time were rounded to 500 seconds and 100 seconds, respectively, for the following calculations. As was discussed in Section 2.3.3 regarding correction to saturation, the activity approaches an asymptote by the equation $A_\infty(t) = R\left(1 - e^{-\lambda t}\right)$. It can be said that, at early times, an exponential function grows linearly as $A_\infty(t) = R\lambda t$ because the exponential term

75

approaches λ at short times. To illustrate this point, Figure 36 is presented. In the figure, both the exponential equation and the linear approximation are plotted with activity normalized to $R = 1$ for simplicity.
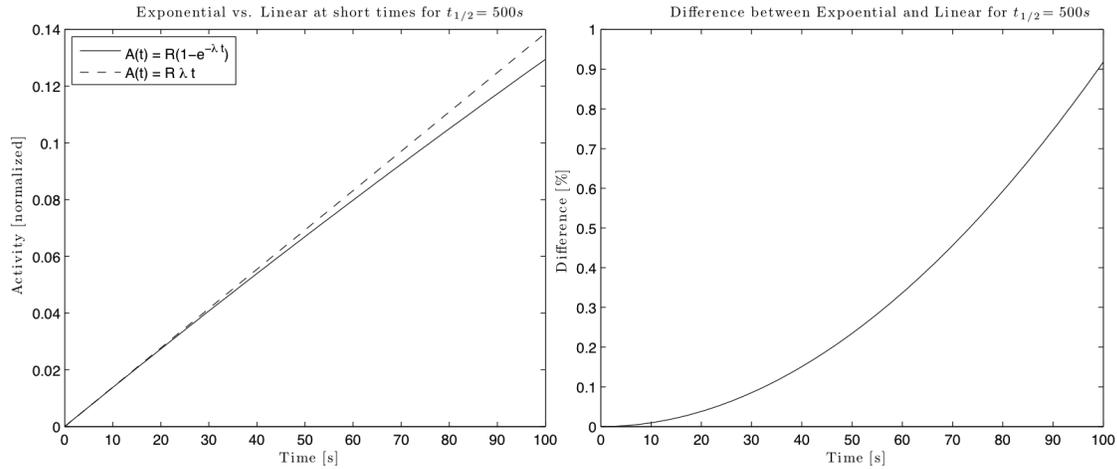
Figure 36. <u>Left:</u> **A comparison of exponential versus linear growth at short times with time, in seconds, on the x-axis and activity in arbitrary units on the y-axis.** <u>Right:</u> **The difference between the exponential and linear equations at all times up to $\overline{100}$ seconds where the y-axis is in units of % difference.**

It is shown that there is little difference between the exponential and linear approximation equations for short times, and the difference is displayed in Figure 36. Even at 100 seconds, the relative difference is less than 1%. Therefore, the approximation that the exponential equation can be described linearly can be considered acceptable.

Further, an understanding of the loss of activity due to decay between pulses can be described mathematically, but only for the first pulse. This is accomplished by splitting up a pulse into irradiation time and decay time. Activity builds up during beam operation and decays while the beam is off. There is a value for activity during irradiation that is equal to the activity after the decay period. During irradiation,

76

the equation describing activity is

$$A(t) = R\left(1 - e^{-\lambda t}\right) \tag{28}$$

as in Section 2.3.3. Knowing this and assuming that the only mechanism removing radioactive atoms from the balance is decay, the activity after decay can be described by

$$A = R\left(1 - e^{-\lambda t_{on}}\right)\left(e^{-\lambda t_{off}}\right), \tag{29}$$

where t_{on} and t_{off} are the beam pulse width and recovery period, respectively. Setting Equation 28 equal to Equation 29 and solving for t yields

$$t = -\frac{1}{\lambda}\ln\left[1 - e^{-\lambda t_{off}} + e^{-\lambda\left(t_{off}+t_{on}\right)}\right], \tag{30}$$

where all the variables on the right are known for beam operating procedures. In the case of a 400 μs pulse at 20 Hz, using Equation 30 yields a time of 3.99972×10^{-3} s. Stated another way, the 400 μs pulse has lost 2.8×10^{-8} s of irradiation time due to decay. Therefore, it can be said that this is the equivalent time of radiation had decay not occurred. Since it has been proven that there is less than a 1% change in linearity at 100 seconds, it can be assumed that the time lost per pulse is not changing over the interval of interest. In 3 hours of total irradiation time with 20 pulses per second, only 0.0059 seconds of irradiation would need to be subtracted from the 108 seconds of irradiation, which is negligible.

A final area of potential error in the system pertains to DGNAA activity correction factors. Many of the correction factors introduced by Koontz [23], were ignored. First, this was done because these are proposed for use when measuring the thermal neutron flux, while this work focused on the full spectrum neutron flux. Also, the scenario is much different. For instance, the irradiated samples were always at least 8 cm

77

from the HPGe detector crystal, as opposed to the situation for Koontz in which the sample sits directly on the detector window. Koontz's equation of interest calculates the activity due to thermal neutrons, A_{th}, as

$$A_{th} = \frac{dN'}{dt} f_g f_w f_e f_\gamma f_{bs} f_s, \tag{31}$$

where each of these correction factors, f, pertain to geometry, counter window absorption, β efficiency, gamma background, β backscattering, and β self-absorption / self-scattering, respectively. However, while these were considered negligible because of the geometry of the detector or were corrected for by the APEX software suite, it does call into question whether these assumptions were valid.

5.1.3 Final Conclusions

In the end, while significant progress was made, a final spectrum could not be resolved based on the work completed. Further work must be accomplished in order to correct the errors inherent in the method.

5.2 Recommendations for Future Work

Without a proper understanding of the spectrum, molding the spectrum to match that of a nuclear weapons environement cannot proceed. Therefore, short-term future work should focus on fixing the current issues in the SAND-II input deck with focus applied first to verifying the initial guess input spectrum. If it is determined that the problems are insurmountable, another method of spectroscopy, such as time-of-flight, may need to be investigated for spectral analysis. Currently, discussions are ongoing at IU CEEM regarding the building of a time-of-flight apparatus attached to the NREP TMR. There is also the potential that the high-voltage transient tripping will be corrected by the purchase of new equipment. This may allow for much longer

78

irradiation intervals, which could help achieve saturation.

The more complex GEANT model must be modified, further refined, and verified. The first question to ask is whether the geometry is the most up-to-date. Then, the errors in the definition of the model geometry must be found and corrected to ensure that the simulation proceeds properly. At this point, the spectrum can be determined and compared with the experimental spectrum obtained by SAND-II or whatever method is found to be acceptable. This will help significantly when attempting to change the spectrum, as changes to the system can be analyzed prior to running experiments.

Once these problems are fixed and the experimental data properly correlates with simulation results, molding of the neutron spectrum can begin. Changing the target configuration, geometry, or material may provide a way to focus more neutrons to a region of experimental interest and increase the total neutron flux. Also, introducing a dense, high-Z material such as a neutron reflector could increase the possibility of backscattering neutrons into the system and reduce system leakage and/or absorption in the borated TMR shell. Increasing the flux, and most importantly shaping the neutron energy spectrum, will be the focus of future work so that the IU CEEM neutron source may be used for radiation effects studies.

Appendix A. Mass Parameters

This appendix provides a listing of the foil data collected prior to irradiation. Mass data was collected using a Sartorius CP224S Digital Scale (S/N: 18450576). This data was subsequently used to calculate the activity per atom, which was supplied to the SAND-II code for analysis.

For the gold foil measurements, $\rho_{Au} = 19.33\frac{g}{cm^3}$ and thickness was $1.27 \times 10^{-3} cm$. The diameter of the foil materials was not measured but calculated by

$$D_i = 2\left[\frac{m_i}{4\pi t_i \rho_i}\right]^{\frac{1}{2}},\tag{32}$$

where m_i is the material's mass, t_i is the thickness, and ρ_i is the density.

The length of a wire, l_i, for a certain wire radius, r_i, was not measured but calculated using the formula

$$l_i = \frac{m_i}{4\pi r_i^2 \rho_i}.\tag{33}$$

Table 10. Gold foil mass parameters for bare gold foil measurement; $m_{avg} = 15.6 \pm 0.5 mg$.

#	Mass (g)	Diameter (cm)
1	0.0148	0.877
2	0.0145	0.868
3	0.0151	0.886
4	0.0159	0.909
5	0.0155	0.897
6	0.0156	0.900
7	0.0154	0.894
8	0.0155	0.897
9	0.0158	0.906
10	0.0160	0.912
11	0.0155	0.897
12	0.0156	0.900
13	0.0158	0.906
14	0.0165	0.926
15	0.0160	0.912
16	0.0156	0.900

Table 11. Gold foil mass parameters for cadmium-covered gold foil measurement; $m_{avg} = 14.9 \pm 0.4 mg$.

#	Mass [g]	Diameter [cm]	t_{Cd} [cm]
1	0.0139	0.850	0.414
2	0.0144	0.865	0.610
3	0.0148	0.877	0.511
4	0.0148	0.877	0.584
5	0.0149	0.880	0.500
6	0.0154	0.894	0.566
7	0.0149	0.880	0.478
8	0.0148	0.877	0.490
9	0.0147	0.874	0.503
10	0.0149	0.880	0.503
11	0.0145	0.868	0.508
12	0.0146	0.871	0.508
13	0.0156	0.900	0.495
14	0.0152	0.889	0.505
15	0.0152	0.889	0.505
16	0.0154	0.894	0.505

Table 12. Pre-measurement parameters for main experimental run (Bare Foil sample set); all materials are wires unless noted otherwise.

Material	Density $\left(\frac{g}{cm^3}\right)$	Location	D (cm)	m (g)	l (cm)
Halstead20101027_01					
Cu	8.940	C	0.10	0.0302	0.42
Ni	8.908	1	0.10	0.0406	0.56
Co	8.900	2	0.10	0.0386	0.53
Cu	8.940	3	0.10	0.0381	0.53
Ni	8.908	4	0.10	0.0378	0.52
Halstead20101027_02					
Ni	8.908	C	0.10	0.0438	0.61
Co	8.900	1	0.10	0.0403	0.56
Cu	8.940	2	0.10	0.0281	0.39
Ni	8.908	3	0.10	0.0367	0.51
Co	8.900	4	0.10	0.0452	0.63
Halstead20101027_03					
Co	8.900	C	0.10	0.0640	0.887
Cu	8.940	1	0.10	0.0537	0.741
Ni	8.908	2	0.10	0.0383	0.530
Co	8.900	3	0.10	0.0571	0.791
Cu	8.940	4	0.10	0.0306	0.422
Halstead20101027_04					
Cu	8.940	C	0.10	0.0715	0.986
Ni	8.908	1	0.10	0.0622	0.861
Co	8.900	2	0.10	0.0327	0.453
Cu	8.940	3	0.10	0.0575	0.793
Ni	8.908	4	0.10	0.0500	0.692
Halstead20101027_05					
Ni	8.908	C	0.10	0.0564	0.781
Co	8.900	1	0.10	0.0450	0.624
Cu	8.940	2	0.10	0.0592	0.817
Ni	8.908	3	0.10	0.0399	0.552
Co	8.900	4	0.10	0.0399	0.553
Halstead20101029_01					
Al	2.700	C	0.10	0.0213	0.97
NONE	N/A	1	N/A	N/A	N/A
Cu	8.940	2	0.10	0.0713	0.98
Ni	8.908	3	0.10	0.0654	0.91
Co	8.900	4	0.10	0.0552	0.77
					Cont. on next page...

Material	Density $\left(\frac{g}{cm^3}\right)$	Location	D (cm)	m (g)	l (cm)
				Cont. from previous page...	
Halstead20101029_03					
Ag[1]	10.500	C	3.18	0.646	0.01
Co	8.900	1	0.10	0.0518	0.72
NONE	N/A	2	N/A	N/A	N/A
Al	2.700	3	0.10	0.0143	0.65
Ni	8.908	4	0.10	0.0743	1.03
Halstead20101103_01					
NONE	N/A	C	N/A	N/A	N/A
Al	2.700	1	0.10	0.0183	0.84
NONE	N/A	2	N/A	N/A	N/A
NONE	N/A	3	N/A	N/A	N/A
Al	2.700	4	0.10	0.0136	0.62
Halstead20101103_02					
NONE	N/A	C	N/A	N/A	N/A
NONE	N/A	1	N/A	N/A	N/A
NONE	N/A	2	N/A	N/A	N/A
Al	2.700	3	0.10	0.0190	0.87
NONE	N/A	4	N/A	N/A	N/A
Halstead20101111_01					
Ni	8.908	C	0.10	0.0810	1.12
Al	2.700	1	0.10	0.0193	0.88
In[1]	7.310	2	1.50	0.3486	0.03
NONE	N/A	3	N/A	N/A	N/A
Co	8.900	4	0.10	0.0731	1.01
Halstead20101111_03					
NONE	N/A	C	N/A	N/A	N/A
In[1]	7.310	1	0.60	0.0194	0.01
Ni	8.908	2	0.10	0.0359	0.50
Ni	8.908	3	0.10	0.0296	0.41
In[1]	7.310	4	0.60	0.0549	0.03
				Cont. on next page...	

Material	Density $\left(\frac{g}{cm^3}\right)$	Location	D (cm)	m (g)	l (cm)
Halstead20101117_01					
In[1]	7.310	C	1.50	0.3345	0.03
Ni	8.908	1	0.10	0.0671	0.93
Al	2.700	2	0.10	0.0182	0.83
In[1]	7.310	3	0.60	0.0218	0.01
Ni	8.908	4	0.10	0.0754	1.04
Halstead20101130_03					
Co	8.908	C	0.10	0.0517	0.72
In[1]	7.310	1	0.60	0.0277	0.01
In[1]	7.310	2	0.60	0.0276	0.01
Al	2.700	3	0.10	0.0265	1.21
In[1]	7.310	4	0.60	0.0235	0.01
Halstead20101201_02					
Co	8.900	C	0.10	0.0482	0.67
Cu	8.940	1	0.10	0.0527	0.73
Ni	8.908	2	0.10	0.0365	0.51
Co	8.900	3	0.10	0.0360	0.50
Cu	8.940	4	0.10	0.0387	0.53
Halstead20101206_01					
Fe[1]	7.870	C	1.27	0.1216	0.01
Fe[1]	7.870	1	1.27	0.1221	0.01
Fe[1]	7.870	2	1.27	0.1221	0.01
Fe[1]	7.870	3	1.27	0.1212	0.01
Fe[1]	7.870	4	1.27	0.1218	0.01
Halstead20101206_02					
Ag[1]	10.5	C	1.27	0.1601	0.01
Ag[1]	10.5	1	1.27	0.1611	0.01
Ag[1]	10.5	2	1.27	0.1606	0.01
Ag[1]	10.5	3	1.27	0.1616	0.01
Ag[1]	10.5	4	1.27	0.1592	0.01
Halstead20101214_02					
Ni	8.908	C	0.10	0.0810	1.12
Al	2.700	1	0.10	0.0193	0.88
In[1]	7.310	2	1.50	0.3486	0.03
Al[2]	2.700	3	0.10	0.0227	1.04
Co	8.900	4	0.10	0.0731	1.01

Note:

[1]Foil

[2]This wire was a cadmium-covered sample ($t_{Cd} = 0.0516cm$).

Table 13. Pre-measurement parameters for main experimental run (Cadmium-Covered Sample set); all materials are wires unless noted otherwise.

Material	Density ($\frac{g}{cm^3}$)	Location	D (cm)	m (g)	l (cm)	t_{Cd} [cm]
Halstead20101111_01c						
Ni	8.908	C	0.076	0.026	0.639	0.051
Al	2.700	1	0.102	0.019	0.886	0.051
In[1]	7.310	2	1.100	0.036	0.005	0.051
NONE	N/A	3	N/A	N/A	N/A	0.051
Co	8.900	4	0.102	0.055	0.761	0.051
Halstead20101123_01c						
Co	8.900	C	0.102	0.048	0.669	0.051
Cu	8.940	1	0.102	0.077	1.060	0.051
Ni	8.908	2	0.102	0.026	0.360	0.051
Cu	8.940	3	0.102	0.059	0.817	0.051
Al	2.700	4	0.102	0.022	0.982	0.051
Halstead20101123_02c						
In[1]	7.310	C	0.600	0.335	0.162	0.052
Co	8.900	1	0.102	0.067	0.930	0.055
Al	2.700	2	0.102	0.018	0.831	0.053
Ni	8.908	3	0.102	0.022	0.302	0.051
Cu	8.940	4	0.102	0.075	1.040	0.055
Halstead20101130_01c						
Co	8.900	C	0.102	0.048	0.669	0.051
Cu	8.940	1	0.102	0.077	1.060	0.051
Ni	8.908	2	0.102	0.026	0.360	0.051
Cu	8.940	3	0.102	0.059	0.817	0.051
Al	2.700	4	0.102	0.022	0.982	0.051
Halstead20101130_02c						
In[1]	7.310	C	0.600	0.335	0.162	0.052
Co	8.900	1	0.102	0.067	0.930	0.055
Al	2.700	2	0.102	0.018	0.831	0.053
Ni	8.908	3	0.102	0.022	0.302	0.051
Cu	8.940	4	0.102	0.075	1.040	0.055
Halstead20101206_03c						
Fe	7.870	C	1.270	0.122	0.012	0.055
Fe	7.870	1	1.270	0.122	0.012	0.053
Fe	7.870	2	1.270	0.123	0.012	0.056
Fe	7.870	3	1.270	0.123	0.012	0.058
Fe	7.870	4	1.270	0.121	0.012	0.052
						Cont. on next page...

					Cont. from previous page...	
Material	**Density** $(\frac{g}{cm^3})$	**Location**	**D (cm)**	**m (g)**	l **(cm)**	t_{Cd}
Halstead20101206_04c						
Ag	10.500	C	1.270	0.161	0.012	0.057
Ag	10.500	1	1.270	0.160	0.012	0.052
Ag	10.500	2	1.270	0.161	0.012	0.052
Ag	10.500	3	1.270	0.159	0.012	0.052
Ag	10.500	4	1.270	0.161	0.012	0.056
Halstead20101214_01c						
Au	10.500	C	1.270	0.028	0.002	0.057
Co	10.500	1	0.102	0.160	1.877	0.052
Co	10.500	2	0.102	0.161	1.891	0.052
Co	10.500	3	0.102	0.159	1.864	0.052
Ni	10.500	4	0.102	0.161	1.888	0.056
Note:						
[1]Designates that this material is a *foil*						

Appendix B. Data Analysis Spreadsheet

This appendix provides an example of the data analysis spreadsheets used to calculate the activity of irradiated materials and make corrections to saturation. All data not displayed in this example can be obtained by requesting it from the author or from the Air Force Institute of Technology's nuclear engineering program.

Figure 37 displays a screen capture of the sheet that kept track of which locations had been irradiated and how many times. Figures 38 and 39 display screenshots of an example of a data analysis spreadsheet used for each irradiation run to analyze the information provided by measurements. The results of these spreadsheets were collected into a final spreadsheet that displayed sets of data for each location. Finally, the example in Figure 40 displays the collection of data for the central wire/foil location.

	A	Center Bare	Center CdCo	Left Bare	Left CdCo	Top Bare	Top CdCo	Bottom Bare	Bottom CdCo	Right Bare	Right CdCo
1		Center		Left		Top		Bottom		Right	
2	Mat'l	Bare	CdCo	Bare	CdCo	Bare	CdCo	Bare	CdCo	Bare	CdCo
3	Cu	X	X	XX	X	X	X	X	X	XX	X
4	Ni	XX	X	X	X	XX	X	X	XX	XXX	X
5	Co	XXX	X	XX	XX	XX	XX	XX	X	XXXX	X
6	In	XX	X	X	X	XX	X	X	X	X	X
7	Al	X	X	XX	X	X	X	XX		X	XX
8	Fe	X	X	X	X	X	X	X	X	X	X
9	Ag	XX	X	X	X	X	X	X	X	X	X
10	Au		X								
11											
12											

Figure 37. One sheet of the irradiation results repository spreadsheet kept track of which locations had been irradiated and how many times.
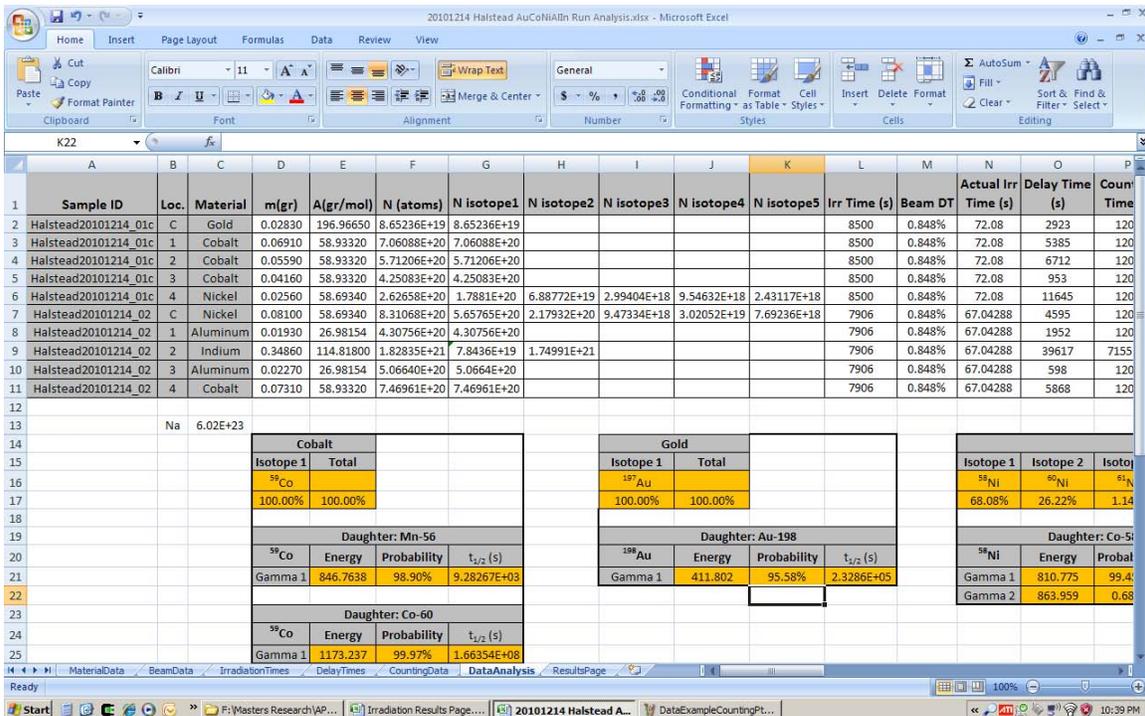
Figure 38. The irradiation spreadsheet kept track of material properties, beam properties, irradiation and delay times, performed calculations of saturation activity, and provided a centralized data repository; this is the first part of the analysis sheet; note, A_{CS} = Saturated Activity

88
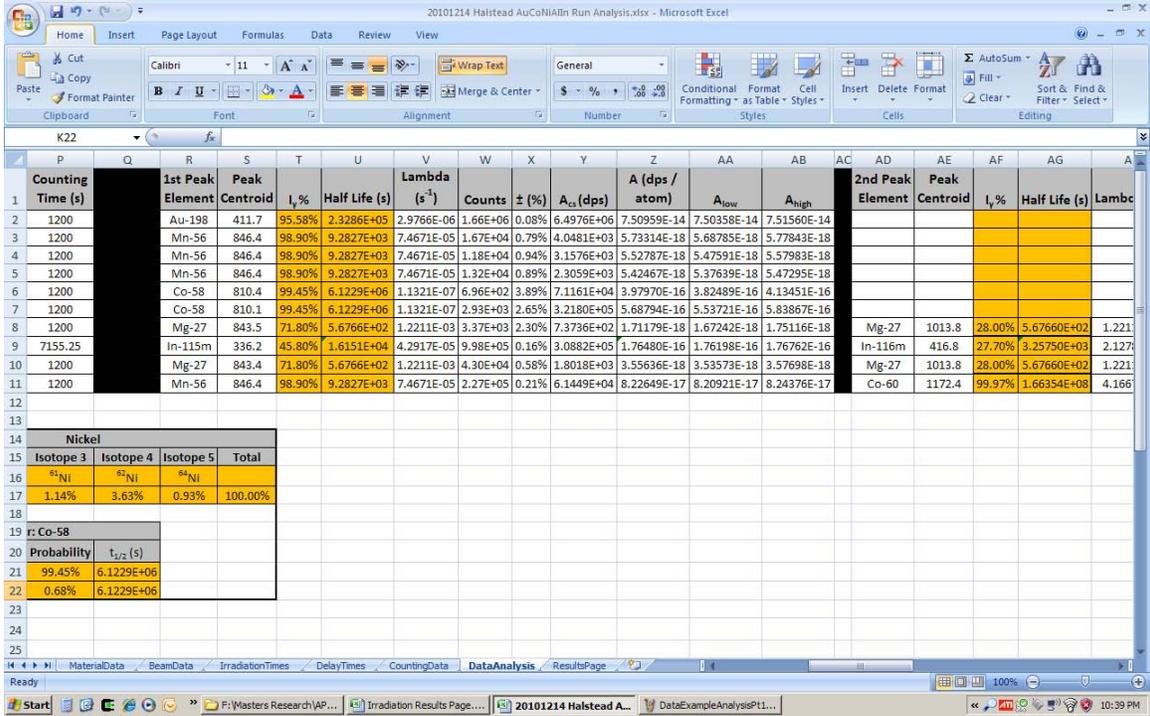
Figure 39. Another snapshot of the irradiation spreadsheet (See Figure 38. This is the second part of the data analysis sheet; each run may or may not have more of these, depending on how many gamma peaks were analyzed.

Figure 40. The spreadsheet that collected all data into a central location provided an easy method of transferring activity data $\left(\text{properly corrected to saturation and in units of } \frac{disintegrations/second}{atom}\right)$ to the SAND-II program input deck.

Appendix C. Raw Activity Data

The data presented in this appendix is the raw data for all measured irradiation samples. Table 14 through Table 18 displays the timing information for all experiments at each irradiation location (please see Figure 28 in Section 4.2.2.1 for reference). Table 19 through Table 28 displays the counts under the gamma curve produced by the HPGe detector NLLS fitting routine with the associated uncertainty.

Table 14. Raw timing data for *center* irradiation location.

Sample ID	Matl.	Irr. Time (sec)	Delay Time (sec)	Counting Time (sec)
20101027_01	Copper	17.145	4403	1200
20101027_02	Nickel	26.529	9054	1200
20101027_03	Cobalt	84.949	5265	1200
20101027_04	Copper	61.030	99026	1200
20101027_05	Nickel	39.780	3561	1200
20101103_01	Sulfur	71.400	379	1200
20101111_01c[1]	Nickel	55.590	1047	1200
20101117_01	Indium	86.688	57123	1200
20101123_01c[1]	Cobalt	82.013	6106	2400
20101130_03	Cobalt	75.302	1947	1200
20101201_02	Cobalt	73.021	2404	1200
20101206_01	Iron	84.537	9301	21600
20101206_02	Silver	162.731	13704	2400
20101206_03c[1]	Iron	105.152	1135	1200
20101214_01c[1]	Gold	72.080	2923	1200
20101214_02	Nickel	67.043	4595	1200
[1]c designates sample is cadmium covered.				

90

Table 15. Raw timing data for *left* irradiation location.

Sample ID	Matl.	Irr. Time (sec)	Delay Time (sec)	Counting Time (sec)
20101027_01	Nickel	17.145	1159	1200
20101027_02	Cobalt	26.529	4397	1200
20101027_03	Copper	84.949	3175	1200
20101027_04	Nickel	61.030	2630	1200
20101027_05	Cobalt	39.780		
20101103_01	Aluminum	71.400	2712	1200
20101111_01c[1]	Aluminum	55.590	2851	1200
20101117_01	Nickel	86.688	2030	1200
20101123_01c[1]	Copper	82.013	3383	1200
20101130_03	Indium	75.302	50557	1200
20101201_02	Copper	73.021	7480	1200
20101206_01	Iron	84.537	2037	1200
20101206_02	Silver	162.731	49640	1200
20101206_03c[1]	Iron	105.152	3863	1200
20101214_01[1]c	Cobalt	72.080	5385	1200
20101214_02	Aluminum	67.043	1952	1200
[1]c designates sample is cadmium covered.				

Table 16. Raw timing data for *top* irradiation location.

Sample ID	Matl.	Irr. Time (sec)	Delay Time (sec)	Counting Time (sec)
20101027_01	Cobalt	17.145	2870	1200
20101027_02	Copper	26.529	6065	1200
20101027_03	Nickel	84.949	1664	1200
20101027_04	Cobalt	61.030	1166	1200
20101027_05	Copper	39.780		
20101103_01	Vanadium	71.400	4214	1200
20101111_01c[1]	Indium	55.590	5030	1200
20101117_01	Aluminum	86.688	362	1200
20101123_01c[1]	Nickel	82.013	8911	2400
20101130_03	Indium	75.302	51986	1200
20101201_02	Nickel	73.021	1081	1200
20101206_01	Iron	84.537	3879	1200
20101206_02	Silver	162.731	7866	1200
20101206_03c[1]	Iron	105.152	7343	1200
20101214_01c[1]	Cobalt	72.080	6712	1200
20101214_02	Indium	67.043	39617	7155.25
[1]c designates sample is cadmium covered.				

Table 17. Raw timing data for *bottom* irradiation location.

Sample ID	Matl.	Irr. Time (sec)	Delay Time (sec)	Counting Time (sec)
20101027_01	Copper	17.145	7635	1200
20101027_02	Nickel	26.529	10743	1200
20101027_03	Cobalt	84.949	7005	1200
20101027_04	Copper	61.030	101763	1200
20101027_05	Nickel	39.780	2094	1200
20101103_01	Sulfur	71.400	5661	1200
20101111_01c[1]	Vanadium	55.590	6312	1200
20101117_01	Indium	86.688	58807	1200
20101123_01c[1]	Copper	82.013		
20101130_03	Aluminum	75.302	399	1200
20101201_02	Cobalt	73.021	3713	1200
20101206_01	Iron	84.537	5991	1200
20101206_02	Silver	162.731	9329	1200
20101206_03c[1]	Iron	105.152	11444	1200
20101214_01c[1]	Cobalt	72.080	953	1200
20101214_02	Aluminum	67.043	598	1200
[1]c designates sample is cadmium covered.				

Table 18. Raw timing data for *right* irradiation location.

Sample ID	Matl.	Irr. Time (sec)	Delay Time (sec)	Counting Time (sec)
20101027_01	Nickel	17.145	6121	1200
20101027_02	Cobalt	26.529	7604	1200
20101027_03	Copper	84.949	88445	1200
20101027_04	Nickel	61.030	4120	1200
20101027_05	Cobalt	39.780	559	1200
20101103_01	Aluminum	71.400	8365	1200
20101111_01c[1]	Cobalt	55.590	26997	1200
20101117_01	Nickel	86.688	3564	1200
20101123_01c[1]	Aluminum	82.013	517	1200
20101130_03	Indium	75.302	53458	1200
20101201_02	Copper	73.021	8851	1200
20101206_01	Iron	84.537	7376	1200
20101206_02	Silver	162.731	10687	1200
20101206_03c[1]	Iron	105.152	13652	1200
20101214_01c[1]	Nickel	72.080	11645	1200
20101214_02	Cobalt	67.043	5868	1200
[1]c designates sample is cadmium covered.				

92

Table 19. Raw counting data for *center* irradiation location (Part 1).

ID	Matl.	Peak 1 cent. (keV)	Peak 1 counts	Peak 1 uncert.	Peak 2 cent. (keV)	Peak 2 counts	Peak 2 uncert.
1027_01	Copper	1345.2	7.524E+03	1.68%			
1027_02	Nickel	810.6	5.923E+02	5.95%			
1027_03	Cobalt	846.6	3.023E+05	0.15%	1172.8	2.991E+05	0.56%
1027_04	Copper	1345.2	1.800E+04	1.09%			
1027_05	Nickel						
1103_01	Sulfur						
1111_01c[1]	Nickel	810.7	2.785E+02	7.86%			
1117_01	Indium	336.3	4.015E+05	0.23%	416.9	4.254E+04	0.96%
1123_01c[1]	Cobalt	846.5	3.568E+04	0.54%	1172.6	2.392E+03	2.19%
1130_03	Cobalt	846.4	2.726E+05	0.20%	1172.6	2.415E+04	0.71%
1201_02	Cobalt	846.4	3.149E+05	0.18%	1172.5	2.855E+04	0.64%
1206_01	Iron	833.9	6.588E+03	3.44%	846.4	6.257E+06	0.04%
1206_02	Silver	657.5	1.924E+05	0.24%	706.4	1.809E+05	0.68%
1206_03c[1]	Iron	846.4	2.286E+05	0.21%			
1214_01c[1]	Gold	411.7	1.655E+06	0.08%			
1214_02	Nickel	810.1	2.929E+03	2.65%			
[1]c designates sample is cadmium covered.							

Table 20. Raw counting data for *center* irradiation location (Part 2).

ID	Matl.	Peak 3 cent. (keV)	Peak 3 counts	Peak 3 uncert.	Peak 4 cent. (keV)	Peak 4 counts	Peak 4 uncert.
1027_01	Copper						
1027_02	Nickel						
1027_03	Cobalt						
1027_04	Copper						
1027_05	Nickel						
1103_01	Sulfur						
1111_01c[1]	Nickel						
1117_01	Indium	1096.8	1.814E+04	1.02%	1292.9	1.494E+04	0.90%
1123_01c[1]	Cobalt	1331.7	2.097E+03	2.41%			
1130_03	Cobalt	1331.6	7.053E+04	0.39%			
1201_02	Cobalt	1331.6	6.396E+04	0.41%			
1206_01	Iron	1098.7	8.090E+03	3.37%	1290.8	5.653E+03	5.96%
1206_02	Silver	763.6	1.674E+05	0.55%	817.7	1.522E+05	1.08%
1206_03c[1]	Iron						
1214_01c[1]	Gold						
1214_02	Nickel						
[1]c designates sample is cadmium covered.							

Table 21. Raw counting data for *left* irradiation location (Part 1).

ID	Matl.	Peak 1 cent. (keV)	Peak 1 counts	Peak 1 uncert.	Peak 2 cent. (keV)	Peak 2 counts	Peak 2 uncert.
1027_01	Nickel						
1027_02	Cobalt	846.6	55659.25	0.43%	Co-60	55061.54	0.43%
1027_03	Copper	1345.2	55080.68	0.62%			
1027_04	Nickel						
1027_05	Cobalt						
1103_01	Aluminum	843.5	1.45E+02	18.08%	1367.9	1.22E+03	2.90%
1111_01c[1]	Aluminum	843.6	6172.7	1.52%	1014.1	5171.43	2.68%
1117_01	Nickel	810.5	5.59E+02	7.48%			
1123_01c[1]	Copper	1345.1	1.18E+03	4.31%			
1130_03	Indium	336.2	1.99E+04	1.06%	416.9	9.51E+03	2.03%
1201_02	Copper	1344.9	1.90E+04	1.06%			
1206_01	Iron	846.4	7.87E+05	0.11%			
1206_02	Silver	657.5	6.84E+04	0.41%	706.4	6.37E+04	1.14%
1206_03c[1]	Iron	846.4	8.56E+04	0.35%			
1214_01c[1]	Cobalt	846.4	1.67E+04	0.79%			
1214_02	Aluminum	843.5	3.37E+03	2.30%	1013.8	3.33E+03	3.50%
[1]*c* designates sample is cadmium covered.							

Table 22. Raw counting data for *left* irradiation location (Part 2).

ID	Matl.	Peak 3 cent. (keV)	Peak 3 counts	Peak 3 uncert.	Peak 4 cent. (keV)	Peak 4 counts	Peak 4 uncert.
1027_01	Nickel						
1027_02	Cobalt						
1027_03	Copper						
1027_04	Nickel						
1027_05	Cobalt						
1103_01	Aluminum						
1111_01c[1]	Aluminum	1367.9	597.04	4.18%			
1117_01	Nickel						
1123_01c[1]	Copper						
1130_03	Indium	1096.7	4.06E+03	2.19%	1292.8	3.46E+03	1.86%
1201_02	Copper						
1206_01	Iron						
1206_02	Silver	763.6	5.91E+04	0.93%	817.7	5.36E+04	1.85%
1206_03c[1]	Iron						
1214_01c[1]	Cobalt						
1214_02	Aluminum	1367.5	1.29E+03	2.83%			
[1]*c* designates sample is cadmium covered.							

94

Table 23. Raw counting data for *top* irradiation location (Part 1).

ID	Matl.	Peak 1 cent. (keV)	Peak 1 counts	Peak 1 uncert.	Peak 2 cent. (keV)	Peak 2 counts	Peak 2 uncert.
1027_01	Cobalt	846.6	7.135E+03	1.23%			
1027_02	Copper	1345.2	9.573E+03	1.50%			
1027_03	Nickel	810.5	1.028E+03	4.94%	1172.8	1.939E+05	0.64%
1027_04	Cobalt	846.6	1.168E+05	0.30%	1172.9	1.155E+05	1.22%
1027_05	Copper						
1103_01	Vanadium						
1111_01c[1]	Indium	336.3	5.290E+04	0.73%	416.9	3.619E+05	0.33%
1117_01	Aluminum	843.6	1.596E+04	0.99%	1014.1	1.360E+04	1.91%
1123_01c[1]	Nickel	810.5	1.510E+03	2.63%			
1130_03	Indium	336.2	1.876E+04	1.10%	416.9	7.787E+03	2.24%
1201_02	Nickel	810.5	6.717E+02	7.55%			
1206_01	Iron	846.4	7.589E+05	0.12%			
1206_02	Silver	657.5	6.989E+04	0.40%	706.4	6.548E+04	1.12%
1206_03c[1]	Iron	846.4	7.989E+04	0.36%			
1214_01c[1]	Cobalt	846.4	1.179E+04	0.94%			
1214_02	Indium	336.2	9.984E+05	0.16%	416.8	2.004E+06	0.14%

[1] c designates sample is cadmium covered.

Table 24. Raw counting data for *top* irradiation location (Part 2).

ID	Matl.	Peak 3 cent. (keV)	Peak 3 counts	Peak 3 uncert.	Peak 4 cent. (keV)	Peak 4 counts	Peak 4 uncert.
1027_01	Cobalt						
1027_02	Copper						
1027_03	Nickel						
1027_04	Cobalt						
1027_05	Copper						
1103_01	Vanadium						
1111_01c[1]	Indium	1096.9	1.521E+05	0.33%	1293	1.261E+05	0.31%
1117_01	Aluminum	1367.9	1.399E+03	4.16%			
1123_01c[1]	Nickel						
1130_03	Indium	1096.7	3.116E+03	2.51%	1292.7	2.685E+03	2.12%
1201_02	Nickel						
1206_01	Iron						
1206_02	Silver	763.6	6.111E+04	0.92%	817.7	5.534E+04	1.79%
1206_03c[1]	Iron						
1214_01c[1]	Cobalt						
1214_02	Indium	1096.5	8.429E+05	0.15%	1292.6	6.993E+05	0.13%

[1] c designates sample is cadmium covered.

Table 25. Raw counting data for *bottom* irradiation location (Part 1).

ID	Matl.	Peak 1 cent. (keV)	Peak 1 counts	Peak 1 uncert.	Peak 2 cent. (keV)	Peak 2 counts	Peak 2 uncert.
1027_01	Copper						
1027_02	Nickel						
1027_03	Cobalt	846.6	195986.86	0.23%	1172.8	193882.18	0.64%
1027_04	Copper	1345.2	12280.25	1.32%			
1027_05	Nickel						
1103_01	Sulfur	846.6	3572.3	1.71%	1172.8	181.05	8.52%
1111_01c[1]	Vanadium						
1117_01	Indium	336.2	1.38E+04	1.27%	416.9	1.94E+03	4.54%
1123_01c[1]	Copper						
1130_03	Aluminum	843.5	5.83E+04	0.51%	1013.9	4.99E+04	0.94%
1201_02	Cobalt	846.4	1.81E+05	0.24%	1172.5	1.86E+04	0.78%
1206_01	Iron	846.4	7.14E+05	0.12%			
1206_02	Silver	657.5	8.14E+04	0.37%	706.4	7.71E+04	1.03%
1206_03c[1]	Iron	846.4	6.14E+04	0.41%			
1214_01c[1]	Cobalt	846.4	1.32E+04	0.89%			
1214_02	Aluminum	843.4	4.30E+04	0.58%	1013.8	3.53E+04	1.03%

[1]*c* designates sample is cadmium covered.

Table 26. Raw counting data for *bottom* irradiation location (Part 2).

ID	Matl.	Peak 3 cent. (keV)	Peak 3 counts	Peak 3 uncert.	Peak 4 cent. (keV)	Peak 4 counts	Peak 4 uncert.
1027_01	Copper						
1027_02	Nickel						
1027_03	Cobalt						
1027_04	Copper						
1027_05	Nickel						
1103_01	Sulfur	1331.9	183.03	0.08			
1111_01c[1]	Vanadium						
1117_01	Indium						
1123_01c[1]	Copper						
1130_03	Aluminum	1367.8	5.07E+03	1.91%			
1201_02	Cobalt	1331.6	2.23E+04	0.70%			
1206_01	Iron						
1206_02	Silver	763.6	7.10E+04	0.85%	817.7	6.58E+04	1.64%
1206_03c[1]	Iron						
1214_01c[1]	Cobalt						
1214_02	Aluminum	1367.6	3.95E+03	1.62%			

[1]*c* designates sample is cadmium covered.

Table 27. Raw counting data for *right* irradiation location (Part 1).

ID	Matl.	Peak 1 cent. (keV)	Peak 1 counts	Peak 1 uncert.	Peak 2 cent. (keV)	Peak 2 counts	Peak 2 uncert.
1027_01	Nickel						
1027_02	Cobalt	846.6	5.751E+04	0.42%	1172.9	5.689E+04	1.33%
1027_03	Copper	1345.2	1.048E+04	1.43%			
1027_04	Nickel						
1027_05	Cobalt	846.6	1.223E+05	0.30%	1172.9	1.210E+05	1.50%
1103_01	Aluminum	1367.9	1.582E+03	2.52%			
1111_01c[1]	Cobalt	846.6	3.572E+03	1.71%	1172.8	1.810E+02	8.52%
1117_01	Nickel	810.6	8.497E+02	4.63%			
1123_01c[1]	Aluminum	843.5	1.611E+04	0.94%	1014	1.352E+04	1.66%
1130_03	Indium	336.2	1.447E+04	1.25%	416.8	4.773E+03	2.91%
1201_02	Copper	1344.9	1.628E+04	1.15%			
1206_01	Iron	846.4	6.431E+05	0.13%			
1206_02	Silver	657.5	7.779E+04	0.38%	706.4	7.263E+04	1.07%
1206_03c[1]	Iron	846.4	5.509E+04	0.43%			
1214_01c[1]	Nickel	810.4	6.958E+02	3.89%			
1214_02	Cobalt	846.4	2.273E+05	0.21%	1172.4	2.647E+04	0.65%

[1] *c* designates sample is cadmium covered.

Table 28. Raw counting data for *right* irradiation location (Part 2).

ID	Matl.	Peak 3 cent. (keV)	Peak 3 counts	Peak 3 uncert.	Peak 4 cent. (keV)	Peak 4 counts	Peak 4 uncert.
1027_01	Nickel						
1027_02	Cobalt						
1027_03	Copper						
1027_04	Nickel						
1027_05	Cobalt						
1103_01	Aluminum						
1111_01c[1]	Cobalt	1331.9	1.830E+02	8.16%			
1117_01	Nickel						
1123_01c[1]	Aluminum	1367.7	1.889E+03	2.34%			
1130_03	Indium	1096.7	2.165E+03	2.98%	1292.8	1.729E+03	2.65%
1201_02	Copper						
1206_01	Iron						
1206_02	Silver	763.6	6.801E+04	0.87%	817.7	6.161E+04	1.69%
1206_03c[1]	Iron						
1214_01c[1]	Nickel						
1214_02	Cobalt	1331.5	2.441E+04	0.67%			

[1] *c* designates sample is cadmium covered.

Appendix D. SAND-II Input Deck

The following is an example of the input deck used with the SAND-II spectrum unfolding code. In this example, there are 15 total foil activities measured, 9 are cadmium-covered. The lines beginning with "ACTS" designate the foil activities (properly corrected to saturation and per atom) in their respective order. The lines following that specify the input initial guess spectrum, first listing the energy data points and second listing the flux data points, in units of differential flux. Please reference the SAND-II user's manual [30] for further information.

```
1 CASES
T BEST CASE SCENARIO
ITERATION
15 FOILS
AL27A
AL27P CADMIUM 1.04263E-03
AL27A CADMIUM 1.04263E-03
CO59A CADMIUM 9.26783E-04
CO59G CADMIUM 9.26783E-04
CU63G
CU63G CADMIUM 1.00093E-03
IN115N
IN115G
IN115G CADMIUM 9.45319E-04
FE56P CADMIUM 1.00093E-03
NI58P
NI58P CADMIUM 9.31417E-04
AG109G
AG109G CADMIUM 1.03336E-03
ACTS 1.11403-17 3.64676-18 1.25246-17
ACTS 8.38512-18 5.54131-15 2.02302-14 8.21599-18 6.39012-16
ACTS 1.47396-13 1.17928-14 2.30237-17
ACTS 1.22445-16 1.45385-16 1.33383-14 5.27655-15
SPECTRUM TABULAR
120 POINTS
ENER 0.0001 0.00012589 0.00015848 0.00019951 0.00025117 0.0003162
ENER 0.00039806 0.00050112 0.00063086 0.00079418 0.0009998 0.0012586
```

```
ENER 0.0015845 0.0019947 0.0025112 0.0031613 0.0039798 0.0050102
ENER 0.0063073 0.0079402 0.009996 0.012584 0.015842 0.019943 0.025107
ENER 0.031607 0.03979 0.050091 0.06306 0.079386 0.099939 0.12581
ENER 0.15839 0.19939 0.25102 0.316 0.39782 0.50081 0.63047 0.7937
ENER 0.99919 1.2579 1.5836 1.9935 2.5097 3.1594 3.9774 5.0071
ENER 6.3035 7.9354 9.9899 12.576 15.832 19.931 25.091 31.588 39.766
ENER 50.061 63.022 79.338 99.879 125.74 158.29 199.27 250.86 315.81
ENER 397.58 500.51 630.09 793.22 998.59 1257.1 1582.6 1992.3 2508.1
ENER 3157.5 3975 5004.1 6299.6 7930.6 9983.9 12569 15823 19919
ENER 25076 31569 39742 50031 62984 79290 99818 125660 158200 199150
ENER 250710 315620 397340 500210 629710 792740 997980 1256400
ENER 1581600 1991100 2506600 3155600 3972600 5001100 6295800 7925800
ENER 9977800 12561000 15813000 19907000 25061000 31549000 39718000
ENER 50000000 62946000 79242000
FLUX 2.2637-08 6.2867-09 4.5312-08 3.5679-08 6.2626-08 1.4501-07
FLUX 3.2185-07 2.1284-07 7.2809-07 2.3078-06 1.8988-06 3.3604-06
FLUX 5.9879-06 1.0343-05 1.842-05 3.2763-05 6.0143-05 7.3917-05
FLUX 0.00011692 0.00018666 0.00028941 0.00051258 0.00062032 0.00089913
FLUX 0.0013635 0.0016411 0.0020836 0.0025084 0.002606 0.0024081
FLUX 0.0021984 0.0015302 0.0010515 0.00064727 0.00047866 0.00043525
FLUX 0.00040945 0.00043708 0.00044892 0.00040064 0.00043498 0.00043121
FLUX 0.00048026 0.00045139 0.00046136 0.0005 0.00050344 0.00050164
FLUX 0.0004866 0.00050087 0.00052828 0.00055536 0.00055733 0.00056814
FLUX 0.00057729 0.00063934 0.0006673 0.00065164 0.00066167 0.00069292
FLUX 0.00071797 0.00071066 0.00076647 0.00080124 0.00081285 0.00085371
FLUX 0.00087221 0.00091692 0.00097701 0.0010049 0.0010034 0.0010561
FLUX 0.0011417 0.0011628 0.001236 0.0012889 0.0013298 0.0014457
FLUX 0.0014213 0.0016285 0.0017407 0.0023035 0.0025093 0.0027716
FLUX 0.0032077 0.0037756 0.0020482 0.00373 0.0050545 0.0062406
FLUX 0.0045692 0.0074794 0.0083703 0.010322 0.012561 0.016133
FLUX 0.019877 0.023459 0.037326 0.039089 0.038634 0.040437 0.040213
FLUX 0.039694 0.037685 0.031339 0.024182 0.020065 0.017517 0.007238
FLUX 2.6168-05 0 0 0 0 0 0 0 0 0
LIMIT 100
DEVIATION 5
DISCARD 100.0
LOW END E
HIGH END FISSION
NORM 1.0-10
PLOT, NO CARDS
SMOOTH 1
```

Bibliography

[1] URL `http://www.nndc.bnl.gov/exfor/endf00.jsp`.

[2] "ROSPEC Data Sheet". URL `http://www.bubbletech.ca/pdfs/BTI_ROSPEC_2010-May-11.pdf`.

[3] "Sun Sets on Sandia Pulsed Reactor". Sandia National Lab News Release, September 2007.

[4] *Nuclear Posture Review Report*. Technical report, United States Department of Defense, 2010.

[5] Agostinelli, S. "GEANT4 - A Simulation Toolkit". *Nucl. Inst. Meth. A*, 506:250–303, 2003.

[6] Amols, H. I., J. F. Dicello, M. Awschalom, L. Coulson, S. W. Johnsen, and R. B. Theus. *Physical Characterization of Neutron Beams Produced by Protons and Deuterons of Various Energies Bombarding Beryllium and Lithium Targets of Several Thicknesses*. Technical Report FERMILAB-Pub-76/102-EXP 1184.000, Fermi National Accelerator Laboratory, 1976.

[7] Baek, I., E. B. Iverson, and J. M. Carpenter. "The Monte Carlo Simulation of Neutron Transmitted and Scattered by Disk Choppers of Various Compositions". *Nucl. Instr. Meth. in Phys. Res. A*, 481(1–3):422–430, April 2002.

[8] Behrens, J. W. *Preparation of Fission Foils for Fission Ionization Chambers Using a Painting Technique*. Technical Report UCRL-51476, University of California Radiation Laboratory, 1973.

[9] Berry, D. T. "Testing and Research Capabilities at the Sandia Fast Pulsed Reactor Facility". *Eleventh Symposium on Space Nuclear Power and Propulstion*, 1994.

[10] Bogdanov, A., V. Anferov, M. Ball, D. V. Baxter, V. P. Derenchuk, A. V. Klyachko, T. Rinckel, P. Sokol, and K. Solberg. "Upgrade of the LENS Proton LINAC: Commissioning and Results". *Proceedings of PAC07*, 2007.

[11] Bramblett, R. L., R. I. Ewing, and T. W. Bonner. "A New Type of Neutron Spectrometer". *Nucl. Instr. Meth.*, 9:1, 1960.

[12] Brede, H. J., G. Dietze, K. Kudo, U. J. Schrewe, F. Tancu, and C. Wen. "Neutron Yields from Thick Be Targets Bombarded with Deuterons or Protons". *Nucl. Instr. Meth. in Phys. Res. A*, 274(1-2):332–344, January 1989.

[13] Brown, F. B., R. F. Barrett, T. E. Booth, J. S. Bull, L. J. Cox, R. A. Forster, T. J. Goorley, R. D. Mosteller, S. E. Post, R. E. Prael, E. C. Selcow, A. Sood, and J. Sweezy. *MCNP Version 5*. Technical Report LA-UR-02-3935, Los Alamos National Laboratory, 2002.

[14] Fernandez-Varea, J.M., R. Mayol, J. Baro, and F. Salvat. "On the Theory and Simulation of Multiple Elastic Scattering of Electrons". *Nucl. Instr. Meth. Phys. Res. B*, 73(4):447 – 473, 1993.

[15] Glasstone, S. and P. J. Dolan. *The Effects of Nuclear Weapons*. DoD/DOE, 3rd edition, 1977.

[16] Goudsmit, S. and J. L. Saunderson. "Multiple Scattering of Electrons. II". *Phys. Rev.*, 58(1):36–42, Jul 1940.

[17] Hippert, F. *Neutron and X-Ray Spectroscopy*. Springer Publishing, 2006.

[18] Howard, W. B., S. M. Grimes, T. N. Massey, S. I. Al-Quarasishi, D. K. Jacobs, C. E. Brient, and J. C. Yanch. "Measurement of the Thick Target ^{9}Be(p,n) Neutron Energy Spectra". *Nucl. Sci. Engr.*, 139:145–160, 2001.

[19] Jastaniah, S. D. and P. J. Sellin. "Digital Techniques for n/ Pulse Shape Discrimination and Capture-Gated Neutron Spectroscopy using Liquid Scintillators". *Nucl. Instr. Meth. in Phys. Res. A*, 517(1-3):202–210, January 2004.

[20] Kapchinsky, I. M. and V. A. Teplyakov. "A Linear Ion Accelerator with Spatially Uniform Hard Focusing". *Prib. Tekh. Eksp.*, 2:19–22, 1970.

[21] Kelly, J.G., P.J. Griffin, and W. C. Fan. "Benchmarking the Sandia Pulsed Reactor-III Cavity: Neutron Spectrum for Electronic Parts". *IEEE Transactions on Nuclear Science*, 40:1418–1425, December 1993.

[22] Knoll, G. F. *Radiation Detection and Measurement*. John Wiley and Sons, Inc., 3rd edition, 2000.

[23] Koontz, R. L., M. A. Greenfield, and A. A. Jarrett. *Absolute Thermal Neutron Determination, Part II: Absolute Beta Counting of Indium Foils*. Technical Report NAA-SR-1137 (Pt. II), North American Aviation, Inc., 1955.

[24] Krane, K. *Introductory Nuclear Physics*. John Wiley and Sons, Inc., 1988.

[25] Lavelle, C. M. *The Neutronic Design and Performance of the Indiana University Cyclotron Facility (IUCF) Low Energy Neutron Source The Neutronic Design and Performance of the Indiana University Cyclotron Facility (IUCF) Low Energy Neutron Source (LENS)*. Ph.D. thesis, Indiana University, March 2007.

[26] Lavelle, C. M. personal communication, 2010.

[27] Lee, Sangjin. personal communication, 2010.

[28] Lewis, H. W. "Multiple Scattering in an Infinite Medium". *Phys. Rev.*, 78(5):526–529, Jun 1950.

[29] Lone, M. A., A. M. Ross, J. S. Fraser, S. O. Schrieber, S. A. Kushneriuk, and W. N. Selander. *Low Energy $^7Li(p,n)^7Be$ Neutron Source (CANUTRON)*. PASS-18-5-R AECL-7413, Chalk River Nuclear Laboratories, 1982.

[30] McElroy, W. N., S. Berg, T. Crockett, and R. G. Hawkins. *A Computer-Automated Iterative Method for Neutron Flux Spectra Determination by Foil Activation*. Vol. 2 AFWL-TR-67-41, Air Force Weapons Laboratory, Kirtland, NM, 1967.

[31] Podgorsak, E. B. *Radiation Physics for Medical Physicists*. Springer-Verlag, 2nd edition, 2010.

[32] von Przewoski, B. "Upgrade of the LENS Proton LINAC: Commissioning and Results". Presentation at HEART Conference, 2008.

[33] von Przewoski, B., D. V. Baxter, A. Bogdanov, S. Clark, V. P. Derenchuk, T. Ellis, C. M. Lavelle, M. B. Leuschner, N. Remmes, T. Rinckel, P. E. Sokol, and T. Turflinger. "The Neutron Radiation Effects Program (NREP) at Indiana University Cyclotron Facility". *Radiation Effects Data Workshop*, 188–190. Ponte Verdi, FL, 2006.

[34] "Qtool: Calculation of Reaction and Threshold Values". URL `http://t2.lanl.gov/data/qtool.html`. [online] `http://t2.lanl.gov/data/qtool.html`.

[35] Reginatto, M. and P Goldhagen. "MAXED, A Computer Code for Maximum Entropy Deconvolution of Multisphere Neutron Spectrometer Data". *Health Phys.*, 77(5):579–583, November 1999.

[36] Roy, S. C. and B. Roy. "Use of Superheated Liquid in Neutron Detection". *Current Science*, 84(4):516–528, February 2003.

[37] Rubinstein, R. Y. and D. P. Kroese. *Simulation and the Monte Carlo Method*. John Wiley and Sons, Inc., Hoboken, NJ, 2nd edition, 2008.

[38] Sisk, D. R., K. L. Swinth, and R. E. Apfel. "Neutron Detection Based on Superheated Materials". *IEEE Trans. Nucl. Sci.*, 37(2):902, 1990.

[39] Vanhavere, F. "A Comparison of Different Neutron Spectroscopy Systems at the Reactor Facility VENUS". *Nucl. Inst. Meth. A*, 476:395–399, 2002.

[40] Various. "Geant4 Physics Reference Manual". Website, 2009.

[41] Wangler, T. P. *RF Linear Accelerators*. Wiley-VCH, New York, NY, 1998.

[42] Webster, J. G. *The Measurement, Instrumentation, and Sensors Handbook.* CRC Press, 1999.

[43] Zijp, W. L., J. H. Board, and H. J. Nolthenius. "Comparison of Neutron Spectrum Unfolding Codes". *Current Status of Neutron Spectrum Unfolding: Proceedings of a Technical Committee Meeting*, IAEA-TECDOC-221, 1–27. International Atomic Energy Agency, Oak Ridge, TN, October 1977.

REPORT DOCUMENTATION PAGE

The public reporting burden for this collection of information is estimated to average 1 hour per response, including the time for reviewing instructions, searching existing data sources, gathering and maintaining the data needed, and completing and reviewing the collection of information. Send comments regarding this burden estimate or any other aspect of the collection of information, including suggestions for reducing this burden to Department of Defense, Washington Headquarters Services, Directorate for Information Operations and Reports (0704-0188), 1215 Jefferson Davis Highway, Suite 1204, Arlington, VA 22202-4302. Respondents should be aware that notwithstanding any other provision of law, no person shall be subject to an penalty for failing to comply with a collection of information if it does not display a currently valid OMB control number.
PLEASE DO NOT RETURN YOUR FORM TO THE ABOVE ADDRESS.

1. REPORT DATE *(DD-MM-YYYY)* 24-03-2011	2. REPORT TYPE Master's Thesis	3. DATES COVERED *(From – To)* Jun 2010 – Mar 2011

4. TITLE AND SUBTITLE Characterization of the Neutron Spectrum at the Indiana University Neutron Source	5a. CONTRACT NUMBER
	5b. GRANT NUMBER
	5c. PROGRAM ELEMENT NUMBER
6. AUTHOR(S) Halstead, Matthew R., Civilian	5d. PROJECT NUMBER
	5e. TASK NUMBER
	5f. WORK UNIT NUMBER

7. PERFORMING ORGANIZATION NAMES(S) AND ADDRESS(S) Air Force Institute of Technology Graduate School of Engineering and Management (AFIT/EN) 2950 Hobson Way WPAFB OH 45433-7765	8. PERFORMING ORGANIZATION REPORT NUMBER AFIT/GNE/ENP/11-M08

9. SPONSORING/MONITORING AGENCY NAME(S) AND ADDRESS(ES) Clark, Steven, Civ, ND-5 Radiation Sciences Chief Engineer, GXM Naval Surface Warfare Center, Crane Division, Building 3334 300 Highway 361 Crane, IN 47522 812-854-1693	10. SPONSOR/MONITOR'S ACRONYM(S) NSWC, Crane
	11. SPONSOR/MONITOR'S REPORT NUMBER(S)

12. DISTRIBUTION/AVAILABILITY STATEMENT
APPROVED FOR PUBLIC RELEASE; DISTRIBUTION UNLIMITED

13. SUPPLEMENTARY NOTES

14. ABSTRACT
The neutron source at the Indiana University Cyclotron Facility produces neutrons via proton bombardment of a natural beryllium (100% ^9Be) target. This source has two beam lines: the LENS and the NREP. The energy spectrum of the neutrons produced on the NREP beam line has not yet been characterized. Through simulation using the GEANT and MCNP particle transport codes as well as neutron activation analysis experiments, an attempt was made to characterize the energy spectrum of the neutron production source. First, the neutron production spectrum of beryllium, simulated using GEANT, was compared with literature; there are significant deviations. Next, foils and wires of pure elements were irradiated in the neutron beam target area and the resulting gamma spectrum measured. This information was used in an unfolding code, SAND-II, to deconvolve the neutron energy spectrum observed at the target. A number of approximations were made to properly account for beam duty time and neutron production anisotropy. The resultants provide a better understanding of the spectrum, but continued work is needed to produce a useful spectrum for the users of the facility.

15. SUBJECT TERMS
neutron spectroscopy, SAND-II, pulsed neutron source, GEANT, Neutron activation analysis

16. SECURITY CLASSIFICATION OF:			17. LIMITATION OF ABSTRACT	18. NUMBER OF PAGES	19a. NAME OF RESPONSIBLE PERSON Dr. James Petrosky
a. REPORT U	b. ABSTRACT U	c. THIS PAGE U	UU	121	19b. TELEPHONE NUMBER *(Include area code)* 937-255-3636 ext. 4562